

Modelling thermochemical processes in protoplanetary disks I: numerical methods.

T. Grassi^{1,2}^{*}, B. Ercolano^{1,2}, L. Szűcs³, J. Jennings⁴^{*}, and G. Picogna^{1,2}

¹Universitäts-Sternwarte München, Scheinerstr. 1, D-81679 München, Germany

²Excellence Cluster Origin and Structure of the Universe, Boltzmannstr.2, D-85748 Garching bei München, Germany

³Max-Planck-Institut für extraterrestrische Physik, Giessenbachstrasse 1, 85748 Garching, Germany

⁴Institute of Astronomy, University of Cambridge, Madingley Road, Cambridge, CB3 0HA, UK

Accepted *****. Received *****, in original form *****

ABSTRACT

The dispersal phase of planet-forming disks via winds driven by irradiation from the central star and/or magnetic fields in the disk itself is likely to play an important role in the formation and evolution of planetary systems. Current theoretical models lack predictive power to adequately constrain observations. We present PRIZMO, a code for evolving thermochemistry in protoplanetary disks capable of being coupled with hydrodynamical and multi-frequency radiative transfer codes. We describe the main features of the code, including gas and surface chemistry, photochemistry, microphysics, and the main cooling and heating processes. The results of a suite of benchmarks, which include photon-dominated regions, slabs illuminated by radiation spectra that include X-ray, and well-established cooling functions evaluated at different temperatures show good agreement both in terms of chemical and thermal structures. The development of this code is an important step to perform quantitative spectroscopy of disk winds, and ultimately the calculation of line profiles, which is urgently needed to shed light on the nature of observed disk winds.

Key words: methods: numerical, astrochemistry, radiative transfer, ISM: photodissociation region, ISM: evolution

1 INTRODUCTION

Planets form from the dust and gas in the circumstellar discs surrounding young, low mass stars. The surface density evolution of these planet-forming disks as well as the mechanisms to finally disperse the gas are likely to play an important role in the formation of planetary systems (e.g. Throop & Bally 2005; Drażkowska et al. 2016; Carrera et al. 2018; Ercolano et al. 2018) and the evolution and migration of young planets (Alexander & Pascucci 2012; Ercolano & Rosotti 2015; Jennings et al. 2018).

Photoevaporation by high energy radiation from the central star as well as magnetic fields are thought to drive vigorous disk winds capable of shaping the evolution and the final dispersal of planet-forming material (see Armitage 2011; Alexander et al. 2014; Ercolano & Pascucci 2017 for recent reviews and Kunitomo et al. 2020; Rodenkirch et al. 2020 for a discussion of the interaction between these processes). However, the efficiency of these winds as predicted

by various models spans several order of magnitudes with theoretical calculations thus far yielding fairly weak observational constraints.

Current studies have been mainly limited to a comparison of the X-ray and EUV-only photoevaporation model (Alexander et al. 2006a,b; Owen et al. 2010, 2011, 2012; Picogna et al. 2019) of forbidden lines from singly ionised neon, neutral oxygen and singly ionised sulphur and nitrogen (e.g. Glassgold et al. 2007; Alexander 2008; Ercolano & Owen 2010; Schisano et al. 2010; Ercolano & Owen 2016) to observational surveys (e.g. Pascucci & Sterzik 2009; Rigliaco et al. 2013; Natta et al. 2014; Simon et al. 2016; Banzatti et al. 2019). Unfortunately, the strong temperature dependence of collisionally excited lines makes them unsuitable to probe the bulk of the wind in the launching regions. Indeed, the theoretical calculations, while being partially successful in matching some of the properties of the observed emission lines, also highlight the need to consider molecular diagnostics which may be able to better sample the wind launching regions. Unfortunately, the predictive power of molecular line intensities and profiles from current theoretical models

*Corresponding author: tgrassi@usm.lmu.de

is not yet sufficient for this task (see discussion in [Ercolano & Pascucci 2017](#)).

This work is the first in a series of papers that will allow modellers to perform synthetic observations of disk winds (magnetic and/or photoevaporative) to identify and analyse diagnostics and determine origins in the disc. Paper II of this series ([Szűcs et al.](#)) describes the relevant chemical processes in disk winds and atmospheres and provides a more detailed description of the currently available chemical codes and their limitations for disk winds.

Here we present PRIZMO¹, a code designed to advance chemical abundances and temperature by a time-step (and the impinging radiation flux accordingly) in a single cell that can be part either of a hydrodynamical or of a multifrequency radiative transfer code. PRIZMO is a flexible yet relatively fast code that can be adapted to a set of astrophysical problems requiring gas- and dust-phase chemistry, photochemistry, and the evaluation of a wide range of thermochemical processes, i.e. heating and cooling.

The study of chemistry in protoplanetary disks, when coupled with radiative transfer and/or hydrodynamics, has been undertaken by several codes with different levels of complexity. Notable examples are [Ilgner & Nelson \(2006\)](#), where chemistry has been employed to determine the ionization fraction of disks, or more recently [Wang & Goodman \(2017\)](#), where winds driven by ultraviolet and X-ray radiation are studied via 2D hydrodynamic simulations coupled with simplified radiative transfer and thermochemistry. [Ilee et al. \(2017\)](#) studied the fragmentation of a disk coupling smoothed particle hydrodynamics, including radiative transfer, and time-dependent chemical evolution, while [Booth & Ilee \(2019\)](#) studied the interplay between chemical evolution and pebble drift in planet-forming disks.

Other well-established numerical frameworks for combined radiative transfer and chemistry in disks include PRODIMO ([Woitke et al. 2009](#)), a code that includes chemistry, X-rays and FUV radiative transfer, heating and cooling, and the capability of determining the equilibrium disk structure; DALI ([Bruderer et al. 2009](#)), a code with dust radiative transfer, chemistry, heating and cooling balance, and disk structure calculation; ANDES ([Akimkin et al. 2013](#)), with 1+1D frequency-dependent radiative transfer, gas-grain chemical evolution, thermal energy balance, and dust grain evolution; [Cleeves et al. \(2013\)](#) developed a 2D disk model of a T-Tauri star system, including FUV and X-ray photons, grain settling, isotope chemistry, and a detailed discussion on the effect of the cosmic-rays; TORUS-3DPDR ([Bisbas et al. 2015](#)) couples hydrodynamics, radiation transport, and PDR chemical and physical calculation, to compare observational and theoretical results.

In Sect. 2 we present the algorithm employed to model chemical reactions in the gas phase and on the dust grains, as well as photochemistry. In Sect. 3 we review the thermochemical processes included in PRIZMO, i.e. cooling and heating, and in Sect. 4 we compare the output from our code with the results from benchmarks of photo-dominated regions. The chemical and thermochemical databases em-

ployed are reported in Sect. 5, the limitations are discussed in Sect. 6, while the summary is in Sect. 7.

2 CHEMISTRY

2.1 Methodology

The core of the code is the DLSODES solver ([Hindmarsh et al. 2005](#)), that evolves the following system of ordinary differential equations (ODE)

$$\frac{dn_i}{dt} = -n_i \sum_j k_{ij}(T, \bar{J})n_j + \sum_{jl} k_{jl}(T, \bar{J})n_j n_l \quad (1)$$

$$\frac{dT}{dt} = (\gamma - 1) \frac{\Gamma(\bar{n}, T, \bar{J}) - \Lambda(\bar{n}, T, T_d)}{k_B n_{\text{gas}}} \quad (2)$$

where n_i is the number density of the i th chemical species (either gas- or dust-phase), k_{ij} is the reaction rate coefficient of the reaction occurring between the i th and the j th chemical species, T is the kinetic temperature of the gas, \bar{n} is the set of the chemical abundances, \bar{J} is the array of the impinging radiation intensities in the different energy bins, T_d is the dust temperature that is solved using radiative equilibrium and described in Sect. 3.9, γ the adiabatic index, Γ and Λ the heating and cooling processes respectively, and k_B is the Boltzmann's constant.

Since PRIZMO is employed as a library called by each cell of a framework code (e.g. hydrodynamical or radiative transfer), it is necessary to provide some information about the global geometry of the problem, depending if multifrequency or standard Draine's field ([Draine 1978](#)) is used. In particular, the framework code needs to provide at runtime the column density of H₂, CO, and N₂ integrated from the radiation source to the evolving cell, as well as the column density of H₂, CO, and H₂O from the current cell toward the radiation escape surface, e.g. the vertical column density when dealing with a protoplanetary disk. These quantities are required to compute self-shielding and cooling efficiency (see Sect. 3.8) when these molecules are present in the network.

The code also needs to know the cosmic-rays ionization rate, and some information about the grain size distribution, i.e. the limits in size, the slope of the power law, and the dust-to-gas mass ratio.

Following the approach of KROME ([Grassi et al. 2014](#)), PRIZMO uses a PYTHON pre-processor to write optimized FORTRAN code, taking advantage of several numerical methods to reduce the global computational footprint. We remark that PRIZMO is designed to evolve chemistry *coupled with thermochemical processes and multifrequency radiation*. When employed to solve standard chemistry (i.e. without coupled thermal processes) it only has similar computational performances to codes that use DLSODES or analogous ODE solvers (e.g. [Semenov et al. 2010](#); [Wakelam et al. 2012](#); [Ruaud et al. 2016](#)).

2.2 Standard gas chemistry

Chemical networks are provided to the code in an easily human-readable format. The reactions and the species are parsed to be converted into corresponding PYTHON objects, that share a set of attributes (mass, charge, etc...) and

¹ The code will be publicly available at <https://bitbucket.org/tgrassi/prizmo/> together with Paper III, where the code will be employed to compute the thermal structure of a disk.

methods (checking mass conservation, parsing textual format, etc. . .). Most of the information are obtained from databases rather than from the user. For example, rate coefficients can be defined directly by their analytical expression, but also obtained from well-established databases, such as KIDA for chemical reaction rates² (Wakelam et al. 2012) or Verner’s astrophysical data collection³ (Verner & Ferland 1996). Analogously, chemical species’ thermochemical properties are from Burcat’s database⁴ (Burcat 1984), and the binding energies are taken from recent works (Penteado et al. 2017).

Chemical reaction rates can be taken from different databases at the same time, as well as overridden with user-defined expressions. Parsing is also very flexible, allowing to include strings in the chemical network written in KIDA and UMIST (McElroy et al. 2013) format at the same time, as well as in its own format.

More details and examples on how the user can customize the chemical network are reported in Appendix A.

2.3 Surface chemistry

PRIZMO is also capable of generating surface-chemistry reactions from the information present in the internal database, as sublimation, freeze-out, and surface-only rate reactions by using the corresponding expressions. In particular, for sublimation we use the Polanyi-Wigner model of thermal desorption (e.g. Stahler et al. 1981)

$$k_{e,i} = \nu_0 \exp\left(-\frac{E_{b,i}}{k_B T_d}\right), \quad (3)$$

where $\nu_0 = 10^{12} \text{ s}^{-1}$ is the Debye frequency (Draine 2009), $E_{b,i}$ the binding energy of the i th species, k_B the Boltzmann’s constant, and T_d the dust surface temperature.

Freeze-out is computed using (Hollenbach & McKee 1979)

$$k_{f,i} = S v_i f_d, \quad (4)$$

where the sticking probability is

$$S = \left(1 + 4 \times 10^{-2} \sqrt{T + T_d} + 2 \times 10^{-3} T + 8 \times 10^{-6} T^2\right)^{-1}, \quad (5)$$

the scaling factor that takes into account the grain size distribution is

$$f_d = \frac{\rho_d}{4/3\pi\rho_0} \cdot \frac{a_{\max}^{p+3} - a_{\min}^{p+3}}{a_{\max}^{p+4} - a_{\min}^{p+4}} \cdot \frac{p+4}{p+3}, \quad (6)$$

v_i is the thermal velocity of the i th species in the gas phase, ρ_d the dust mass density, ρ_0 its bulk density, a_{\min} and a_{\max} are the limits of the dust size distribution radii, that is represented by a power-law with exponent p (Mathis et al. 1977), i.e. $\varphi(a) \propto a^p$, normalized in order to have $\rho_d = 4/3\pi\rho_0 \int_a a^3 \varphi(a) da$, where the integral is defined in the range a_{\min} to a_{\max} .

At the present stage, we employed the generic sticking coefficient in Eq. (5), aware that more accurate expressions are available for specific grain substrates and molecules

(e.g. Leitch-Devlin & Williams 1985), and we refer the reader to Sect. 3 of Cuppen et al. (2017). We plan to upgrade this aspect of the code in the future.

For the reactions that occur on the surface of grains we use (Hocuk & Cazaux 2015)

$$k_{s,ij} = P_a \nu_0 f_d \frac{a_p^2}{4\pi} \left[\exp\left(-q_h \frac{E_{b,i}}{k_B T_d}\right) + \exp\left(-q_h \frac{E_{b,j}}{k_B T_d}\right) \right], \quad (7)$$

where $a_p = 3 \times 10^{-8} \text{ cm}$ is the distance between binding sites, $q_h = 2/3$ is the hopping factor, and the tunnelling probability $P_a = \exp(-4\pi a_r \sqrt{2\mu_{ij} E_a}/h)$ is determined by the size of the barrier $a_r = 10^{-8} \text{ cm}$, μ_{ij} is the reduced mass of the two reactants, E_a the energy barrier that depends on the specific reaction, and h the Planck’s constant. Here we assume that the binding energies of the species are not affected by the presence of ices on the substrate (i.e. grains are considered always bare), and that the products obtained from the chemical reactions on the surface of the grains remains on the surface (see e.g. Cazaux et al. 2016; Minissale et al. 2016), and that can only return to the gas phase via evaporation, with the rate in Eq. (3). We are aware of these limitations, and we are planning to upgrade this particular aspect of the code in a future release.

We do not include automatic reaction rate creation for photodesorption, but the processes can be added manually in the chemical network, following for example Hollenbach et al. (2009), that consider a species-dependent yield (see Andersson & van Dishoeck 2008; Cuppen et al. 2017 for a discussion on the uncertainties). Analogously, cosmic-rays desorption is not included, but can be added using e.g. Hasegawa & Herbst (1993) based on Leger et al. (1985).

2.4 H₂ formation on dust

To model the formation of molecular hydrogen on dust grains we follow the results of the model described in Cazaux & Spaans (2009), that include physisorption and chemisorption, tunnelling, and realistic grain surface barriers. For a single silicate dust grain of radius a , the rate coefficient of the reaction $\text{H}+\text{H}\rightarrow\text{H}_2$ is

$$k_d = \frac{1}{2} \pi a^2 n_d S \epsilon_d v_g, \quad (8)$$

where the gas thermal velocity of the hydrogen atoms is

$$v_g = \sqrt{\frac{8k_B T}{\pi m_H}}, \quad (9)$$

and

$$\epsilon_d = \frac{1}{1 + \epsilon_1} + \frac{\epsilon_2}{\epsilon_3}, \quad (10)$$

with k_B the Boltzmann constant, m_H the mass of the hydrogen, and

$$\begin{aligned} \epsilon_1 &= \frac{16 T_d}{E_{\text{ch}} - E_s} \exp\left(-\frac{E_{\text{ph}}}{T_d} + 4 \times 10^9 a_{\text{pc}} \sqrt{E_{\text{ph}} - E_s}\right), \\ \epsilon_2 &= 2 \exp\left(\frac{E_s - E_{\text{ph}}}{E_{\text{ph}} + T}\right), \\ \epsilon_3 &= \left(1 + \sqrt{\frac{E_{\text{ch}} - E_s}{E_{\text{ph}} - E_s}}\right)^2, \end{aligned} \quad (11)$$

² <http://kida.astrophy.u-bordeaux.fr/>

³ <http://www.pa.uky.edu/~verner/atom.html>

⁴ <http://garfield.chem.elte.hu/Burcat/burcat.html>

with $E_{\text{ph}} = 700$ K, $E_{\text{ch}} = 1500$ K, $E_{\text{s}} = -1300$ K, $a_{\text{pc}} = 1.7 \times 10^{-10}$ m (Cazaux, private comm.). For a dust model as the one discussed in Sect. 2.3, Eq. (8) can be written as

$$k_{\text{d}} = f_{\text{d}} S \epsilon v_{\text{g}} = f_{\text{d}} \Phi_{\text{d}}(T, T_{\text{d}}), \quad (12)$$

where f_{d} is defined in Eq. (6), and Φ_{d} is precomputed during the preprocessor stage and linearly interpolated at runtime as a function of T and T_{d} . A more extensive discussion on the formation of molecular hydrogen on dust grains can be found e.g. in Wakelam et al. (2017).

2.5 Photochemistry

The code is designed to compute photochemistry rates either with a radiation spectrum with multiple bins discretized in energy, or with visual extinction A_{v} and radiation intensity (Habing factor) G_0 normalized over the Draine's FUV field (Draine 1978; Tielens 2010).

2.5.1 Multiple energy bins

To compute the reaction rates we use the classic approach that assumes

$$k_{\text{ph}} = \frac{1}{h} \int_{E_{\text{th}}}^{\infty} \frac{\sigma(E) J(E)}{E} dE, \quad (13)$$

where the E_{th} is the energy threshold of the given reaction, σ its cross section, and J the radiation, and where the chosen discretization of the integral takes advantage of arrays vectorization as explained in Appendix B. Cross sections are taken from different sources, Verner & Ferland (1996) for atomic data, and Heays et al. (2017) for molecular data (see Sect. 5).

In the case of energy binning, the user decides the energy range $[E_{\text{min}}, E_{\text{max}}]$ and the number of bins N_{ph} that will be employed. Analogously to what the Monte Carlo radiative transfer code MOCASSIN (Ercolano et al. 2003, 2005) does, to ensure that the cross-section value at the threshold is correctly captured, the code automatically divides the selected energy range, first using three bins per each reaction energy threshold (e.g. hydrogen has $E_{\text{th,H}} = 13.6$ eV), i.e. E_{th} and $E_{\text{th}} \pm \Delta E$, where $\Delta E = 0.00408$ eV, and then distributing the remaining grid points on a log-spaced grid from E_{min} to E_{max} . The code verifies that at least $N_{\text{ph}}/2$ grid points are used for the log-spaced grid. Once the grid has been defined, it remains fixed, the cross-sections are integrated over this, and every process that deals with radiation (see e.g. photoelectric heating) is optimized accordingly.

2.5.2 Visual extinction approximation

If the shape of the radiation resembles a Draine field

$$J(E) = h (1.658 \times 10^6 E^2 - 2.152 \times 10^5 E^3 + 6.919 \times 10^3 E^4), \quad (14)$$

with E in eV and $J(E)$ in $\text{eV cm}^{-2} \text{Hz}^{-1} \text{s}^{-1}$, it is safe to assume that the reaction rates are simply represented by the following expression

$$k_{\text{ph}} = G_0 a_i \exp(-c_i A_{\text{v}}), \quad (15)$$

where G_0 uniformly scales the radiation without changing the energy distribution, a_i is the result of integrating Eq. (13) with Eq. (14), and c_i a coefficient that takes into account the attenuation due to dust (including scattering) as a function of the visual extinction A_{v} (Heays et al. 2017).

This approach is not the default, but it is useful when the code needs to be coupled with frameworks that employ frequency-independent radiation, e.g. most hydrodynamical codes. Note that using Eq. (15) instead of Eq. (13) is slightly faster, since there is no significant overhead from solving the integral (however computational time is reduced by use of vectorization, see Appendix B).

2.5.3 Self-shielding

Both in the cases described in Sect. 2.5.1 and 2.5.2, it is necessary to take into account the self-shielding for H_2 and CO photodissociation reactions. To be fully consistent the code should compute the absorption from the rovibrational lines of these two molecules, but for the present set-up this operation is too computationally expensive, since it involves a large number of molecular lines (Visser et al. 2009). We therefore make use of approximations that are designed to work with the Draine field. In particular for H_2 we use (Draine & Bertoldi 1996; Richings et al. 2014)

$$f_{\text{H}_2} = \frac{1 - \omega}{(1 + x/b_5)^a} \exp[-5 \times 10^{-7}(1 + x)] + \frac{\omega}{\sqrt{1 + x}} \exp(-8.5 \times 10^{-4} \sqrt{1 + x}) \quad (16)$$

where

$$\omega = 0.013 \left[1 + \left(\frac{T}{2700 \text{ K}} \right)^{1.3} \right]^{1/1.3} \exp \left[- \left(\frac{T}{3900 \text{ K}} \right)^{14.6} \right] \quad (17)$$

and $x = N_{\text{H}_2}/N_{\text{crit}}$, where $N_{\text{crit}} = 1.3 \times 10^{14} \left[1 + \left(\frac{T}{600 \text{ K}} \right)^{0.8} \right]$ and $a = 1.4$ when $T < 3000$ K, $N_{\text{crit}} = 2 \times 10^{14}$ and $a = 1.1$ when $T < 4000$ K, and finally, $N_{\text{crit}} = 10^{14} \left(\frac{T}{4760 \text{ K}} \right)^{-3.8}$ and $a = \left(\frac{T}{4500 \text{ K}} \right)^{-0.8}$ otherwise.

For CO self-shielding we employ the table from Visser et al. (2009), where $f_{\text{CO}}(N_{\text{H}_2}, N_{\text{CO}})$ is interpolated on the fly from a table. Analogously, N_2 self-shielding is computed by interpolating the expression $f_{\text{N}_2}(N_{\text{H}_2}, N_{\text{N}_2}, N_{\text{H}})$ from the tables described in Heays et al. (2014) (details employed for these and CO tables are discussed in Sect. 5).

Accounting for self-shielding, the rates for the photodissociation of molecular hydrogen, CO, and N_2 are respectively

$$k_{\text{H}_2} = k_{\text{H}_2}^{\text{ref}} f_{\text{H}_2} \quad (18)$$

$$k_{\text{CO}} = k_{\text{CO}}^{\text{ref}} f_{\text{CO}} \quad (19)$$

$$k_{\text{N}_2} = k_{\text{N}_2}^{\text{ref}} f_{\text{N}_2}, \quad (20)$$

where k_i^{ref} can be computed with Eq. (13) or Eq. (15).

2.5.4 Attenuation of the radiation

Multifrequency radiation $J(E)$ is attenuated to $J'(E)$ after crossing a cell of size Δx accordingly to the chemical com-

position as

$$J'(E) = J(E) \exp \left[-\kappa(E)\rho_d\Delta x - \sum_i \sigma_i(E)n_i\Delta x \right], \quad (21)$$

where the sum runs over the chemical species which have photochemical cross sections $\sigma_i(E)$ and abundance n_i , while the dust with mass density ρ_d and frequency-dependent dust opacity $\kappa(E)$ further attenuates the radiation. Dust opacity is loaded at runtime after being pre-calculated during the preprocessor stage. For simplicity, we do not include additional processes in the attenuation of $J(E)$, such as absorption resulting in molecular excitations. In the attenuation of $J(E)$ we also do not include H_2 and CO self-shielding from photodissociation, that are taken into account following Sect. 2.5.3.

2.6 Optimizing the calculation of rate coefficients

When thermochemistry is computed in the same set of differential equations, rate coefficients need to be evaluated every time the solver calls the function that evaluates their right-hand side, i.e. Eq. (1). This represents a considerable computational overhead, since many reaction rates contain complex (i.e. expensive) operations (logarithms, exponentials, etc.). To overcome this problem we have divided the rate coefficients into three categories: (i) interpolatable in a log-log space as a function of the gas temperature, (ii) not-interpolatable because the rate depends on other factors than just the gas temperature, and (iii) single-evaluated, that do not depend on the temperature and that can be evaluated only during the first call to the solver, as for example photochemistry and cosmic ray ionization. The code automatically splits the reactions into these three groups in order to minimize the cost of rate evaluation at runtime.

3 THERMOCHEMISTRY

PRIZMO is capable of evolving the temperature of the gas and the dust consistently with the chemical evolution and with the impinging radiation by using the set of processes that are described in this Section. Solving the thermal component together with the chemical evolution ensures the consistency of the results, but on the other hand reduces the computational efficiency, since the ODE system in Eq. (1) and Eq. (2) might become numerically stiffer, and the Jacobian becomes less sparse. For these reasons it is fundamental that all the expressions of the thermochemical processes included (as well as their derivatives) do not present discontinuities with respect to the variables of the ODE system (e.g. temperature and density). This holds, for example, for CO and H_2O cooling tables, or for the rate coefficients that are involved in the collisional excitation cooling.

3.1 Cosmic-ray heating

Cosmic-ray heating is modelled following the approach of Galli & Padovani (2015), where the main sources of energy are H and H_2 reactions with cosmic rays, namely

$$\Gamma_{\text{CR}} = \zeta \left(5.5 \times 10^{-12} n_{\text{H}} + 2.5 \times 10^{-11} n_{\text{H}_2} \right), \quad (22)$$

where ζ is the cosmic-rays ionization rate per H_2 molecule in s^{-1} , n_{H} and n_{H_2} are atomic and molecular hydrogen number densities in cm^{-3} , and the total heating Γ_{CR} is in units of $\text{erg s}^{-1} \text{cm}^{-3}$.

3.2 PAH heating

Heating from polycyclic aromatic hydrocarbons (PAH) is related to the dust photoelectric heating, however, due to the uncertainties in the PAH chemistry we use (Bakes & Tielens 1994; Woitke et al. 2009)

$$\Gamma_{\text{PAH}} = 10^{-22} f_{\text{PAH}} y_{\text{H}} \varepsilon_{\text{PAH}} G_0 \mathcal{D}, \quad (23)$$

where $f_{\text{PAH}} = 0.02$ (default value), y_{H} is the H nuclei number density, \mathcal{D} is the dust-to-gas mass ratio, and

$$\varepsilon_{\text{PAH}} = \frac{0.0487}{1 + 4 \times 10^{-3} x_{\text{PAH}}^{0.73}}, \quad (24)$$

with $x_{\text{PAH}} = G_0 \sqrt{T} n_e^{-1}$, where n_e is the electron number density. The resulting heating is in units of $\text{erg s}^{-1} \text{cm}^{-3}$.

3.3 Photochemical heating

The machinery for the photochemical heating depends on the impinging multifrequency radiation $J(E)$ and it is conceptually similar to the one employed to calculate the reaction rates in Sect. 2.5.1, therefore it takes advantage of the same vectorization optimization. In particular for each photochemical rate we have

$$\Gamma_{\text{ph},i} = \eta_{\text{ph}} n_i \int_{E_{\text{ph},i}}^{\infty} \frac{J(E)\sigma_i(E)}{E} (E - E_{\text{ph},i}) dE, \quad (25)$$

that can be written as

$$\Gamma_{\text{ph},i} = \eta_{\text{ph}} n_i \left[\int_{E_{\text{th}}}^{\infty} J(E)\sigma_i(E) dE - E_{\text{ph},i} k_{\text{ph}} \right], \quad (26)$$

where the first term of the right hand side will be vectorized according to Appendix B and k_{ph} is the corresponding photochemical rate, that has been already computed following Sect. 2.5.1. $E_{\text{ph},i}$ is the energy threshold of the photochemical reaction rate (e.g. 13.6 eV for H photoionization).

The fraction of energy deposited in the gas depends on the ionization fraction $x_e = n_e/n_{\text{tot}}$ as

$$\eta_{\text{ph}} = 10^{0.25452 \log(x_e)}, \quad (27)$$

a fit with 10% error with respect to the expression from Xu & McCray (1991), employed here to have a function with no discontinuities in x_e .

3.4 Dust photoelectric heating

Photoelectric heating is computed taking into account the multifrequency radiation spectrum as in Weingartner & Draine (2001) and Weingartner et al. (2006). In principle, this requires the code to track the charge distribution on the dust grains. For the sake of the code efficiency, and to reduce the complexity of the algorithms, we compute the charge distributions assuming equilibrium between the charged grains and the ions and the electrons in the gas phase (Okuzumi 2009; Fujii et al. 2011; Grassi et al. 2019).

The main processes involved are described by (i) k_{pe} the

rate at which the valence band electrons are removed from the grains, (ii) k_{pd} the rate of the photodetachment of the attached electrons, and (iii) the electrons-grains interactions k_e , as well as (iv) the cations-grains k_i . These components are employed to solve the linear system for $n(Z)$

$$n(Z) \left[k_{\text{pd}}(Z) + k_{\text{pe}}(Z) + \sum_i n_i k_i \right] = n(Z+1) n_e k_e \quad (28)$$

and $\sum_Z n(Z) = n_d$ to find the fraction of grains $n(Z)$ in each charged state Z (see Appendix C), where the sum on i runs over the cations⁵.

Once the fraction of grains in each charged level Z is known, it is possible to compute the total heating by using

$$\Gamma_{\text{pe}}(Z) = n(Z) \frac{\int_a \varepsilon(a, Z) \int_E J(E) E^{-1} \Phi(a, E, Z) dE da}{h \int_a a^p da}, \quad (29)$$

with the integrals ranging from a_{min} to a_{max} and E_{th} to infinity, and

$$\Phi(a, E, Z) = \pi a^{2+p} Q(a, E) Y(a, E, Z), \quad (30)$$

where Q is the dust absorption coefficient⁶, that is computed by PRIZMO with Mie theory (Bohren & Huffman 1983), as discussed in Sect. 5. The yield of the process is

$$Y(a, E, Z) = y_2(a, E, Z) \min [y_0(a, E, Z) y_1(a, E), 1]. \quad (31)$$

For y_1 and y_2 we follow the equations from Weingartner et al. (2006), while for y_0 we employ the data from Fig. 2 of their paper. We assume silicate grains with work function $W = 8$ eV, band gap $E_{\text{bg}} = 5$ eV, photo attenuation length $l_a(\lambda) = \lambda [4\pi \text{Im}(m_\lambda)]^{-1}$, where m_λ is the refractive index at $\lambda = c(Eh)^{-1}$, electron escape length $l_e = 10^{-7}$ cm if $E < 211$ eV or $3.27 \times 10^{-11} (E/10^5 \text{ eV})^{1.5}$ cm otherwise (Weingartner et al. 2006).

In Eq. (29) the efficiency is

$$\varepsilon(a, Z) = 6 \int_{E_{\text{min}}}^{E_{\text{max}}} \frac{E(E - E_{\text{low}})(E_{\text{high}} - E)}{(E_{\text{high}} - E_{\text{low}})^3} y_2(a, E, Z) dE \quad (32)$$

with $E_{\text{min}} = 0$ when $Z \geq 0$ and from Eq. (3) of Weingartner et al. (2006) otherwise, while $E_{\text{max}} = E - E_{\text{pet}} + E_{\text{min}}$ with E_{pet} that depends on the valence band ionization potential; see Eq. (2) and Eq. (6) in Weingartner et al. (2006). When $Z < 0$ we have $E_{\text{low}} = E_{\text{min}}$ and $E_{\text{high}} = E_{\text{max}}$, and $Z \geq 0$ instead $E_{\text{low}} = -(Z+1)e^2/a$ and $E_{\text{high}} = E - E_{\text{pet}}$, with e the elementary charge.

The rate at which electrons are removed from the dust grains $k_{\text{pe}}(Z)$ is given by Eq. (29) without the efficiency term ε and $n(Z)$, and the photodetachment rate is

$$k_{\text{pd}}(Z) = \frac{\int_E J(E) E^{-1} \int_a a^{p+2} \sigma_{\text{pd}}(E) da dE}{h \int_a a^p da} \quad (33)$$

where the photo detachment cross-section $\sigma_{\text{pd}}(E)$ is as in Eq. (20) of Weingartner & Draine (2001) with $\Delta E = 3$ eV.

⁵ The maximum charge $|Z|$ is defined by the user during the pre-processor stage. In the benchmarks presented in Sect. 4 we use $Z = [-4, 4]$.

⁶ In principle, the optical properties of a grain depend on the charge Z (Bohren & Huffman 1983; Li & Draine 2000), but large uncertainties in the process make it hard to constrain its dependence on Z .

Finally, the interplay with the gas-phase is controlled by the electron-grain interactions rates

$$k_e = S_e v_g(T) \frac{\int_a a^{p+2} \tilde{J}_e(a, T, Z) da}{\int_a a^p da}, \quad (34)$$

where $S_e = 0.1$ is the electron sticking efficiency, that here we assume to be constant, but that in principle is a function of the grain size, the dust temperature, and the depth of the potential well between electrons and grains due to polarization interaction (see Draine & Sutin 1987; Nishi et al. 1991; Bai 2011; Grassi et al. 2019). The thermal speed of the electrons is

$$v_g = \sqrt{\frac{8k_B T}{\pi m_{e^-}}}, \quad (35)$$

where m_{e^-} is the mass of the electron, and $\tilde{J}_e(a, T, Z)$ is a function that depends on the size and on the charge of the dust grain's reaction-partner, and represents the integral of the electron-grain capture cross section with the Maxwellian velocity distribution (see Sect. II.b and III.a of Draine & Sutin 1987). To find k_i for cations we use Eq. (34), assuming unitary sticking efficiency and v_g with the mass of the specific cation instead of the electron, and using $\tilde{J}_i(a, T, Z)$. i.e. the analogue of \tilde{J}_e for cations.

As discussed in the previous sections, we pre-compute the coefficients of the integrals to benefit from vectorization at runtime.

3.5 Atomic radiative cooling

We compute the radiative atomic cooling by assuming equilibrium between the electronic levels of the atoms included in the chemical network. This is solved by considering the collisional excitation with hydrogen atoms and electrons present in the gas, or other atoms and molecules (e.g. He and H₂) when collisional rate coefficients are available. For a generic atom with N levels we have to satisfy the following linear system (Maio et al. 2007; Woitke et al. 2009)

$$n_i \sum_{j \neq i} R_{ij} = \sum_{j \neq i} n_j R_{ji}, \quad (36)$$

where $R_{ij} = A_{ij} + \sum_\ell k_{ij}^\ell n_\ell$ if $i > j$ and $R_{ij} = \sum_\ell k_{ij}^\ell n_\ell$ if $i < j$. The Einstein coefficients A_{ij} represent the spontaneous transition probability from the i th to the j th level, while k_{ij}^ℓ is the excitation rate coefficient to excite the atom from the i th to the j th level, with the ℓ th collider that has number density n_ℓ . The temperature-dependent rate coefficients for collisions with protons and electrons are from the CHIANTI database (see Sect. 5). The rates are linearly interpolated at runtime to reduce the computational cost. Additional rate coefficients for the first three excited levels of C⁽⁺⁾, Si⁽⁺⁾, and O⁽⁺⁾ and H₂ and He colliders are included as in KROME (Grassi et al. 2014). To solve the linear system in Eq. (36) we employ `dgesv` from LAPACK⁷ for systems with more than three levels, otherwise we solve the system analytically to save computational time.

When the level population n_i of each excited level is computed, the resulting cooling of a transition $i \rightarrow j$ of

⁷ <http://www.netlib.org/lapack/>

a given atom is $\Lambda_{\text{line},ij} = n_i \Delta E_{ij} A_{ij} \beta_{ij}$, where ΔE_{ij} is the difference in energy between the levels, and the escape probability is (Tielens 2010)

$$\beta_{ij} = \left[4\tau_{ij} \sqrt{\ln \left(\frac{\tau_{ij}}{\sqrt{\pi}} \right)} \right]^{-1}, \quad (37)$$

if $\tau_{ij} > 7$ and

$$\beta_{ij} = \frac{1 - e^{-2.34\tau_{ij}}}{4.68\tau_{ij}}, \quad (38)$$

otherwise. Here

$$\tau_{ij} = \frac{c^3 h^3}{8\pi} \frac{A_{ij} n_i}{\Delta E_{ij}^3 d_z v} \left(\frac{n_j g_i}{n_i g_j} - 1 \right), \quad (39)$$

where $d_z v$ is the velocity gradient along the z -component, for which we have assumed that the velocity gradient is large when compared to the thermal motion, as discussed in Tielens (2010).

This approach allows not only to compute the total collisional emission cooling by summing $\Lambda_{\text{line},ij}$ for all the available electronic transitions, but also to have access to the individual emission lines from the gas and to track their evolution in time. At runtime we do not compute the shape of the emitted line (Lorentzian, Gaussian, etc.), since it is not relevant to compute the total cooling.

This formalism is valid also for molecules, for which we employ the data from the LAMDA database⁸ (Schöier et al. 2005) to evaluate the emission of the different lines, while for cooling we use precomputed tables, as discussed in the next sections.

3.6 Bremsstrahlung cooling

Bremsstrahlung produces cooling from the radiation emitted by charged particles that decelerate when deflected by the presence of other charged particles, and following Cen (1992) we have

$$\Lambda_{\text{BS}} = g_{\text{ff}} n_{e^-} \sum_i Z_i^2 n_i, \quad (40)$$

where $g_{\text{ff}} = 1.5$ is the Gaunt factor, n_{e^-} the number density of the electrons, Z_i and n_i the charge and the number density of the i th species, and where i runs on all the ions. The final cooling Λ_{BS} is in units of $\text{erg s}^{-1} \text{cm}^{-3}$.

3.7 Chemical cooling/heating

Chemical cooling or heating is determined by the endothermicity or exothermicity of the given reaction, i.e. if a given reaction requires or releases energy. The amount of energy for the ℓ th reaction is determined by the reaction rate coefficient (k_ℓ) and the difference in enthalpy of formation (ΔH_f°) between the reactants and the products that have abundances n_i , $\Lambda_{\text{chem},\ell} = k_\ell \left(\sum_{\text{react}} \Delta H_{f,i}^\circ - \sum_{\text{prod}} \Delta H_{f,i}^\circ \right) \prod_{\text{prod}} n_j$. In principle, analogously to the rate coefficient, the enthalpy of formation of a given compound is a function of the temperature, that can be computed by using the thermodynamic

data in polynomial form (Burcat 1984). However, since the variation with the temperature of ΔH_f° is small compared to the variation of k_ℓ , and since several coefficients have a limited temperature range, we compute only the standard enthalpy, i.e. when $T = 298.15$ K. The coefficients of the polynomials are taken from Burcat's table and employed to compute ΔH_f° during the preprocessor stage, and multiplied at runtime by the reaction rate and the abundances of the products.

Since not all the reactions play a key role in the total Λ_{chem} , it is possible to limit this calculation to a subset of chemical species, for example by employing only hydrogen- and helium-based species, that are the most abundant. Collisional ionization are always considered endothermic, while cation-electron recombinations cooling is $\Lambda_{\text{rec},i} = k_{\text{B}} T k_{i,e^-} n_i n_{e^-}$, where k_{i,e^-} is the corresponding rate coefficient (Cen 1992).

3.8 CO and H₂O cooling

In principle, molecular cooling can be computed by using the same machinery presented in Sect. 3.5, however given the availability of pre-computed tables, we prefer to use the latter to reduce the computational time. CO cooling (and analogously water cooling) is obtained from the tables in the Appendix B of Omukai et al. (2010), that are functions of the gas temperature (T), the amount of H nuclei (y_{H}), and of the column density from the cell to the surface from which the radiation is assumed to escape (N_{CO}), namely $\Lambda_{\text{CO}} = n_{\text{CO}} f_{\text{CO}}(T, y_{\text{H}}, N_{\text{CO}})$. These tables are computed using the method of Neufeld & Kaufman (1993), that assume level populations in statistical equilibrium, and employ data from the LAMDA database. These are interpolated at runtime by PRIZMO using a three-dimensional linear interpolation routine. The limits of the CO tables are $T = [3, 10^4]$ K, $y_{\text{H}} = [10^{-2}, 10^{14}] \text{cm}^{-3}$, and $N_{\text{CO}} = [10^{-18}, 10^{25}] \text{cm}^{-2}$. Analogously, water cooling limits are $T = [10, 10^3]$ K, $y_{\text{H}} = [10^2, 10^{12}] \text{cm}^{-3}$, and $N_{\text{H}_2\text{O}} = [10^9, 10^{19}] \text{cm}^{-2}$. Outside these limits we assume that when the gas temperature is small the cooling is inefficient, since collisions are less effective in populating the ro-vibrational molecular levels, as well as when the local density is high. Conversely, when the column density toward the escape surface is small the cooling is more efficient, since the radiation is capable of escaping from the simulation domain.

3.9 Dust cooling and dust temperature

When the temperature of the dust is less (greater) than the temperature of the gas, the dust cools (heats) the surrounding medium, since they are in radiation balance (Kirchhoff's law) and exchange kinetic energy with molecules and atoms. In particular, we assume (Hollenbach & McKee 1979; Draine 2011; Grassi et al. 2017)

$$\Gamma_{\text{em}} = \Gamma_{\text{abs}} + \Lambda_{\text{d-g}}, \quad (41)$$

where the first term is the thermal radiative emission of the dust, the second the absorption that depends on the impinging radiation, and the last term is the dust-gas thermal exchange. In our case these terms are

$$\Gamma_{\text{em}} = \frac{4\pi}{h} \int_E B(E, T_d) \int_a Q(a, E) a^{2+p} da dE, \quad (42)$$

⁸ <https://home.strw.leidenuniv.nl/~moldata/>

where $B(E, T_d)$ is the spectral radiance of a blackbody with temperature T_d . The integral on the energy is computed in the range of validity of Q , while the integral on the dust size from a_{\min} to a_{\max} that we assume constant during the evolution. Γ_{em} is pre-computed and interpolated at runtime as a function of T_d only. The absorption

$$\Gamma_{\text{abs}} = \frac{\pi}{h} \int_E J(E) \int_a Q(a, E) a^{2+p} da dE, \quad (43)$$

depends on the impinging radiation $J(E)$, and since this term changes at runtime, we take advantage of vectorization as discussed in Appendix B, pre-computing the rest of the integral. In this case the limits on the integral on energy are the limits of $J(E)$ as defined by the problem boundary conditions (the energy grid is not changed during runtime). Finally, the interaction between gas and dust is

$$\Lambda_{\text{d-g}} = 2\pi v_g k_B \alpha_g n_{\text{gas}} (T - T_d) \int_a a^{p+3} da, \quad (44)$$

where the definition of the gas thermal velocity v_g in Eq. (35) has μm_p , i.e. the mean molecular weight of the gas and the mass of the proton, instead of just the mass of the electron, and $\alpha_g = 0.5$ takes into account the composition of the gas to evaluate the momentum exchange (Hollenbach & McKee 1979), but that in our case we keep constant.

Since Γ_{em} and $\Lambda_{\text{d-g}}$ both depend on T_d , we can use Eq. (41) and a bisection method to find T_d .

With T_d known, and by considering that Eq. (44) holds for a single grain, the total cooling/heating from the dust-gas interaction is

$$\Lambda_{\text{d-g}} = \frac{\mu m_p n_{\text{gas}} \mathcal{D}}{4/3\pi\rho_0 \int_a a^{3+p} da} (\Gamma_{\text{em}} - \Gamma_{\text{abs}}), \quad (45)$$

where m_p , and where we use the difference of emission and absorption instead of Eq. (44) directly to avoid employing the difference $(T - T_d)$ that may cause instability in the solver due to the high precision required (Grassi et al. 2017).

3.10 H₂ cooling

For molecular hydrogen cooling we employ temperature-dependent look-up tables for several colliders, including H, H⁺, H₂ (assuming ortho-to-para ratio 3:1), e⁻, and He. These tables (Glover & Abel 2008; Glover 2015) are represented by piece-wise functions (see Appendix D), each one defined on a T_{\min} to T_{\max} range, that are multiplied to have continuous derivative by a window function

$$\omega(x) = 10^{200[\sigma_f(x, -0.2, 50)\sigma_f(-x, -1.2, 50) - 1]}, \quad (46)$$

where

$$x = \frac{\log(T) - \log(T_{\min})}{\log(T_{\max}) - \log(T_{\min})}, \quad (47)$$

and

$$\sigma_f(x, x_0, s) = \frac{10}{10 + \exp[-s(x - x_0)]}. \quad (48)$$

From the look-up functions (see Appendix D) we obtain the low-density cooling $\Lambda_{\text{H}_2}^{\text{low}}$ that determines the total cooling as

$$\Lambda_{\text{H}_2} = n_{\text{H}_2} \frac{\Lambda_{\text{H}_2}^{\text{low}} \Lambda_{\text{H}_2}^{\text{high}}}{\Lambda_{\text{H}_2}^{\text{low}} + \Lambda_{\text{H}_2}^{\text{high}}} \quad (49)$$

where the high-density cooling $\Lambda_{\text{H}_2}^{\text{high}}$ is reported in Appendix E.

4 BENCHMARK MODELS

To verify the results produced by the code we selected a set of benchmarks that cover a reasonable range of physical and chemical configurations. We limit the present tests to photon-dominated regions (PDR), and we do not provide any disk benchmark, since these will be discussed more in detail in Paper III (despite PDRs representing a good model to test disk physics, see e.g. Bruderer et al. 2009). PDRs are studied in detail, especially by the well-established benchmark⁹ of Röllig et al. (2007) (R07), where several codes are compared, and where detailed instructions and final results are provided in order to reproduce the results with relative ease. The PDR models discussed in R07 have two different densities ($n_{\text{gas}} = 10^3 \text{ cm}^{-3}$ and $n_{\text{gas}} = 10^{5.5} \text{ cm}^{-3}$) and two radiation intensities ($\chi = 10$ and $\chi = 10^5$), and the resulting four models are evolved at constant or variable temperature (i.e. with or without thermochemistry). In our case we evolve the models with variable temperature, for $n_{\text{gas}} = 10^3 \text{ cm}^{-3}$ and radiation intensity $\chi = 10$ (V1) and for $n_{\text{gas}} = 10^{5.5} \text{ cm}^{-3}$ and $\chi = 10^5$ (V4). Instead of using A_v -based photochemical reaction rates as in R07, we employ the multi-frequency binning with the same Draine-like radiation source valid in the range 6 to 13.6 eV.

We then extend these tests to a wider radiation spectrum that includes X-rays (XDR), and verify the validity of our results by comparing the temperature profiles obtained by Picogna et al. (2019) using a pure atomic chemical network. Finally, we validate our calculation of the equilibrium cooling function for different temperatures as in Gnat & Ferland (2012).

4.1 PDR: Röllig et al. (2007) V1

We follow the set-up of R07, that consists of a 1D semi-infinite slab with constant gas density $n_{\text{gas}} = 10^3 \text{ cm}^{-3}$, and with a plane-parallel radiation source emanating from the left side of the simulation box, that has a Draine spectrum with $\chi = 10$. We scaled the the CO and H₂ photoionization rates to match the one required by the benchmark at $A_v = 0$. The cosmic-rays ionization rate is $\zeta = 5 \times 10^{-17} \text{ s}^{-1}$, and the initial conditions for the chemistry are as in Tab. 1. The grain size distribution has $p = -3.5$ in the range $a_{\min} = 5 \times 10^{-7} \text{ cm}$, $a_{\max} = 2.5 \times 10^{-5} \text{ cm}$, silicate grains with $\rho_0 = 3 \text{ g cm}^{-3}$, and dust-to-gas mass ratio $\mathcal{D} = 10^{-2}$ (see also Sect. 2.3). The factor for the self-shielding in Eq. (16) is $b_5 = 1$, while the velocity gradient for the escape probability in Eq. (39) is $d_z v = 10^{-5} \text{ s}^{-1}$. We use 200 logarithmically-spaced grid points from $A_v = 10^{-6}$ to $A_v = 30$, assuming $A_v = 6.289 \times 10^{-22} N$ (as in R07), where N is the column density in units of cm^{-2} . We do find equilibrium chemistry and temperature by running our code for $t = 10^8 \text{ yr}$, and we manually verify that equilibrium is reached. The ending time is explicitly set longer than the expected equilibrium time.

⁹ <https://zeus.ph1.uni-koeln.de/site/pdr-comparison/>

	V1	V4	cooling	XDR	Units
n_{gas}	1(3)	1(5.5)	1	1(2)	cm^{-3}
ζ	5(-17)	5(-17)	-	5(-17)	s^{-1}
χ	10	1(5)	0	see text	-
n_{H_2}	0.5	0.5	-	-	n_{gas}
n_{H}	0	0	0.8	1	n_{gas}
n_{H^+}	0	0	0.2	0	n_{gas}
n_{O}	3(-4)	3(-4)	4.41(-4)	4.90(-4)	n_{gas}
n_{O^+}	0	0	4.90(-5)	0	n_{gas}
n_{C}	1(-4)	0	0	2.69(-4)	n_{gas}
n_{C^+}	0	1(-4)	2.69(-4)	0	n_{gas}
n_{He}	1(-1)	1(-1)	8.51(-2)	8.51(-2)	n_{gas}
n_{Ne^+}	0	0	8.51(-5)	0	n_{gas}
n_{Ne}	0	0	0	8.51(-5)	n_{gas}
n_{N}	0	0	0	6.76(-5)	n_{gas}
n_{S^+}	0	0	0	1.32(-5)	n_{gas}
n_{Mg^+}	0	0	0	3.98(-5)	n_{gas}
T	50	50	see text	50	K

Table 1. Initial conditions values for the different code benchmarks. Electron abundance n_{e^-} is initialized to ensure global charge neutrality. Note $a(b) = a \times 10^b$.

For this benchmark the formation of molecular hydrogen on dust grains is not modelled as in Sect. 2.4, but we employ the expression in R07, i.e. $k_d = 3 \times 10^{-18} \sqrt{T_d} \text{ cm}^3 \text{ s}^{-1}$. This is because our aim is to test thermal processes and photochemistry, and the different expressions for H_2 formation on grains will considerably affect the final results, complicating their analysis (especially for V4, described later). Additional details about this issue in Appendix F.

We employ a different chemical network, but using the same species as in the original benchmark, namely, H, H^+ , H_2 , H_2^+ , H_3^+ , O, O^+ , OH^+ , OH, O_2 , O_2^+ , H_2O , H_2O^+ , H_3O^+ , C, C^+ , CH, CH^+ , CH_2 , CH_2^+ , CH_3 , CH_3^+ , CH_4 , CH_4^+ , CH_5^+ , CO, CO^+ , HCO^+ , He, He^+ , e^- . The chemical network is reported in Appendix G and it will be discussed in detail in Paper II. Our aim is to fairly reproduce the gas and dust temperature profile, within the spread found by the different codes that participated in the original benchmark.

We report the dust and grain temperature profiles as a function of the visual extinction A_v in the top left panel of Fig. 1, where the dashed line is the model ‘‘UCL-chem’’ from R07, model V1. We note that the gas temperature profile is similar to the one from the benchmark, still keeping in mind that their profile is higher with respect to the other models, so that our temperature profile is within the uncertainty from the benchmark. Analogously, the dust temperature profile presents similar features and it is within the results obtained by the codes of the R07 benchmark. Compared to the findings in Hocuk et al. (2017), we obtained a lower dust temperature at higher A_v (e.g. their Fig. 3); we verified that this discrepancy derives from the different radiation field employed, i.e. a Draine field limited to 6–13.6 eV in our case, while they include a broader spectrum that accounts for the mid-infrared component, as discussed in their Sect. B. The behavior of T_d at higher densities is discussed in Appendix H.

To understand the temperature profile, we report in the top right panel of Fig. 1 the cooling and the heating rates for each component. At low A_v the dominating coolant is `cool_atomic`, i.e. the collisional radiative cooling from atoms

which is several orders of magnitude greater than the second most important `cool_dust`, while the heating is controlled by photoelectric, chemical, and PAH heating. In the inner part of the cloud (higher A_v), CO and water are the main coolants, while heating is dominated by cosmic-rays (`heat_CR`) and chemical heating.

The bottom panels of Fig. 1 show the cooling and heating functions at different temperatures, keeping the chemical composition fixed, and in principle the intersection between the two total functions should indicate the equilibrium temperature. We note that for $A_v = 10^{-6}$, atomic line cooling is the dominating factor, apart from a small bump around 10^4 K, where molecular hydrogen cooling is dominating (note again that in this plot for all the temperatures the chemical composition is the one found at the equilibrium for the given A_v). At lower temperatures heating is dominated by photoelectric, chemical, and PAH heating, while at higher temperatures photoionization and photodissociation heating becomes dominant. For $A_v = 30$, CO cooling dominates at lower temperatures, then is replaced by molecular hydrogen cooling from around 100 K to 3×10^4 K, where CO cooling becomes dominating again. The plateau in the CO cooling function there is given by the limits on our cooling functions. However, in this temperature range we do not expect to find a relevant amount of CO molecules. We could then expect that dust cooling becomes dominant, depending on whether the grains are thermally coupled with the gas.

We also compare the results from some of the key chemical species, as for example the transition between molecular and atomic hydrogen (left panel of Fig. 2), OH, O_2 , and CO (middle panel), and electrons and H^+ (right panel). We note a general agreement with R07, apart from some discrepancies that come from the different chemical network and from the slightly different temperatures found. As expected, the molecular component is predominant at higher A_v , and the ionization fraction is larger at lower A_v , where radiation is dominating.

4.2 PDR: Röllig et al. (2007) V4

This test has the same initial conditions as the V1 discussed in Sect. 4.1 (see Tab. 1), apart from the total gas density and the radiation field strength, that now are $n_{\text{gas}} = 10^{5.5} \text{ cm}^{-3}$ and $\chi = 10^5$. We also assume that carbon is fully ionized, to avoid problems during the first call of the photoelectric heating routine (however, even a small amount of electrons is sufficient). This does not affect the final results, which reach equilibrium in any case.

Analogously to Sect. 4.1, in the left panel of Fig. 3 we report the temperature profile as a function of the visual extinction for the gas and the dust components, for which we find general agreement between our results and the results from R07 (here the reference is ‘‘Cloudy’’). As discussed in the case V1, our results agree with the range of values found amongst the benchmark codes. The temperatures are higher at lower visual extinctions, i.e. closer to the radiation source, and become lower when moving inside the cloud.

This trend is confirmed when in the right panel of Fig. 3 we plot the detailed cooling and heating functions as a function of the visual extinction; in the outer part of the slab, photoelectric heating and dust cooling are the two dominant components, while in the inner part chemical heating dom-

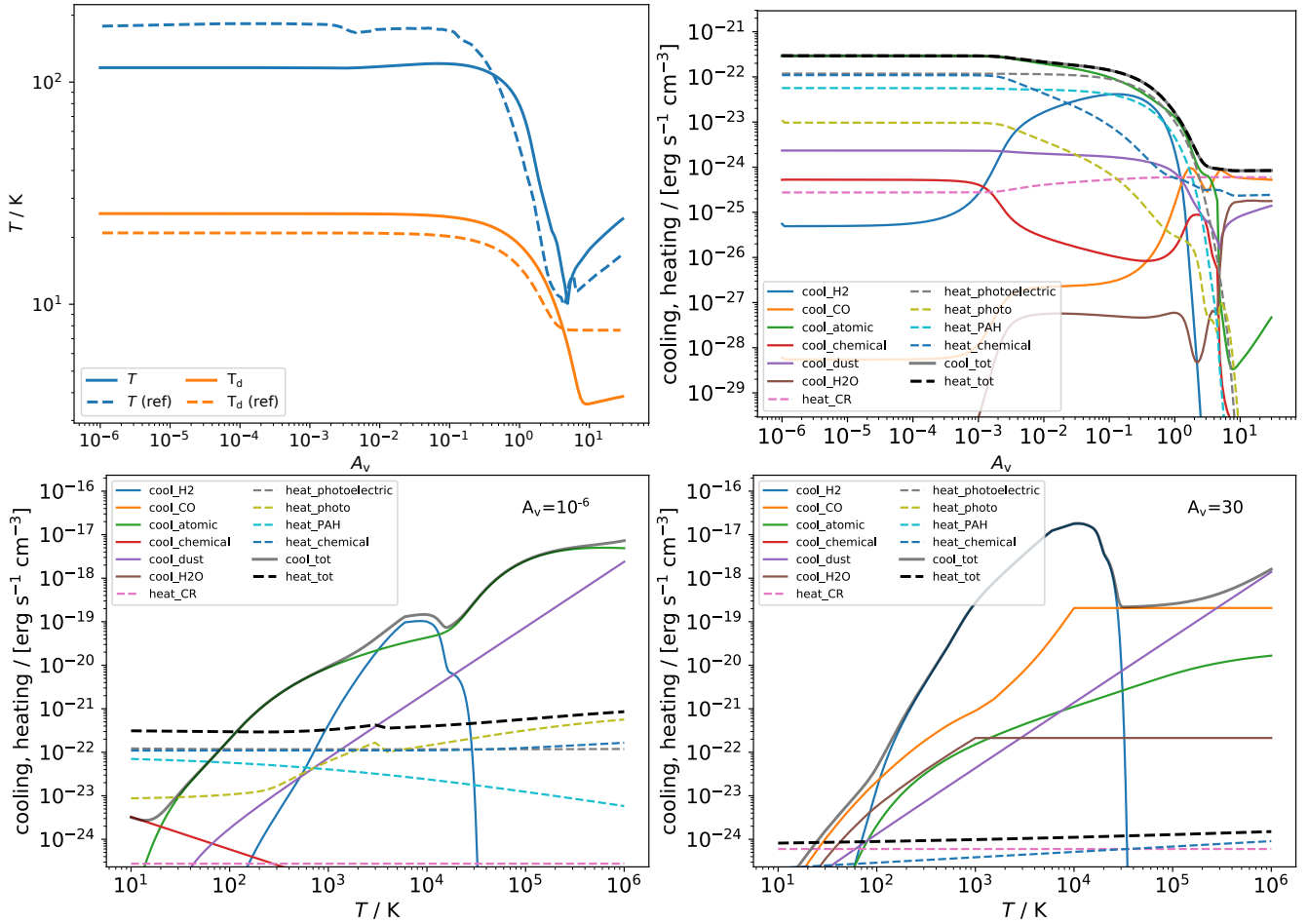


Figure 1. Model V1. **Top left panel:** gas (blue) and dust (orange) temperature profiles as a function of the visual extinction A_v . Solid lines are the results from our code, while dashed indicate model “UCL-chem” from R07. **Top right panel:** cooling (solid) and heating (dashed) functions at different visual extinction values. Grey solid and black dashed lines respectively indicate the sum of the cooling (`cool_tot`) and heating terms (`heat_tot`). The functions are respectively molecular hydrogen cooling (`cool_H2`), CO cooling (`cool_CO`), collisional radiative atomic cooling (`cool_atomic`), dust-gas interaction cooling (`cool_dust`), water cooling (`cool_H2O`), cosmic-ray heating (`heat_CR`), photoelectric heating from dust grains (`heat_photoelectric`), photoionization heating (`heat_photo`), heating from PAH (`heat_PAH`), and chemical heating (`heat_chemical`). **Bottom left panel:** cooling (solid) and heating (dashed) functions as at different temperatures at $A_v = 10^{-6}$, keeping the chemical abundances fixed to the values found at equilibrium by the code at the given A_v . Grey solid and black dashed lines respectively indicate the sum of the cooling (`cool_tot`) and heating terms (`heat_tot`). **Bottom right panel:** cooling (solid) and heating (dashed) functions as at different temperatures at $A_v = 30$, keeping the chemical abundances fixed to the values found at equilibrium by the code at the given A_v . Grey solid and black dashed lines respectively indicate the sum of the cooling (`cool_tot`) and heating terms (`heat_tot`).

inates. The transition between these two zones is controlled by the collisional atomic radiative cooling, and photoelectric and chemical heating.

Our results agree with the benchmark for where atomic hydrogen becomes molecular (Fig. 4, left panel), but we find that differences in the gas temperature affect the chemistry, as shown by the middle panel of Fig. 4, where O_2 , OH, and CO have lower molecular abundances because of the higher temperature, while in the inner part of the slab the abundances agree better, since temperatures are comparable. In the right panel of Fig. 4 the source of the difference we found at lower A_v can be explained by the fact that the ionization is controlled mainly by the photoionization rates, that are similar to the ones from the benchmark, while the discrepancies found in H^+ are due to the different gas-phase rate coefficients from our chemical network.

4.3 Cooling benchmark

The aim of the cooling benchmark is to compute the equilibrium chemistry at different gas temperatures and evaluate the cooling, in order to obtain a function similar to Fig. 3 in Gnat & Ferland (2012) (see also Sutherland & Dopita 1993). Their results show the contributions of the different chemical species to the total cooling, and consist of a temperature-dependent cooling function from $T = 10^4$ to 10^8 K for atomic species in chemical equilibrium without any impinging external radiation. Since we extend our test to $T < 10^4$ K, we compare our results also to Fig. 4 from Maio et al. (2007), that produced an analogous cooling function that includes that specific temperature range. We employ H, He, C, O, Ne, and no dust, with the initial abundances as in Tab. 1, and we evolve the system for

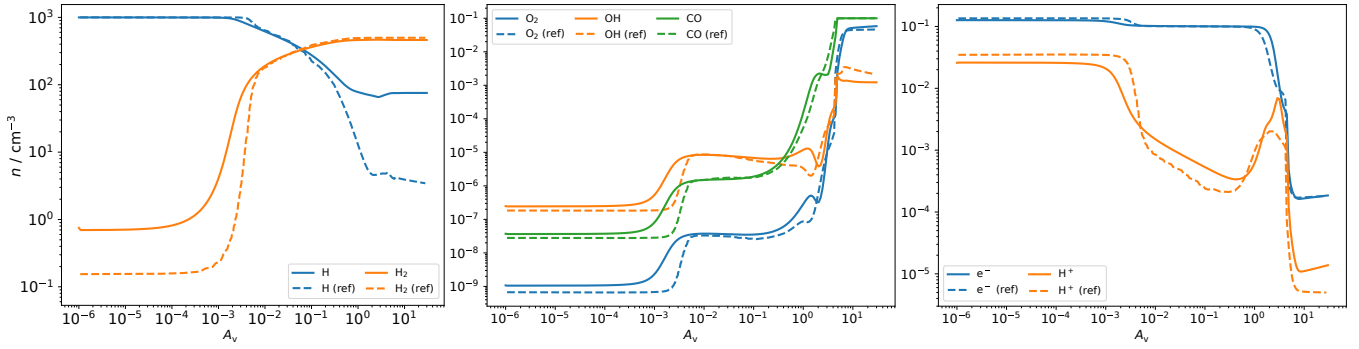


Figure 2. Model V1. **Left panel:** H (blue), and H₂ (orange) density profiles as a function of the visual extinction A_v . Solid lines are the results from our code, while dashed indicate model “UCL-chem” from R07. **Middle panel:** O₂ (blue), OH (orange), and CO (green) density profiles as a function of the visual extinction A_v . Solid lines are the results from our code, while dashed indicate model “UCL-chem” from R07. **Right panel:** e⁻ (blue) and H⁺ (orange) density profiles as a function of the visual extinction A_v . Solid lines are the results from our code, while dashed indicate model “UCL-chem” from R07.

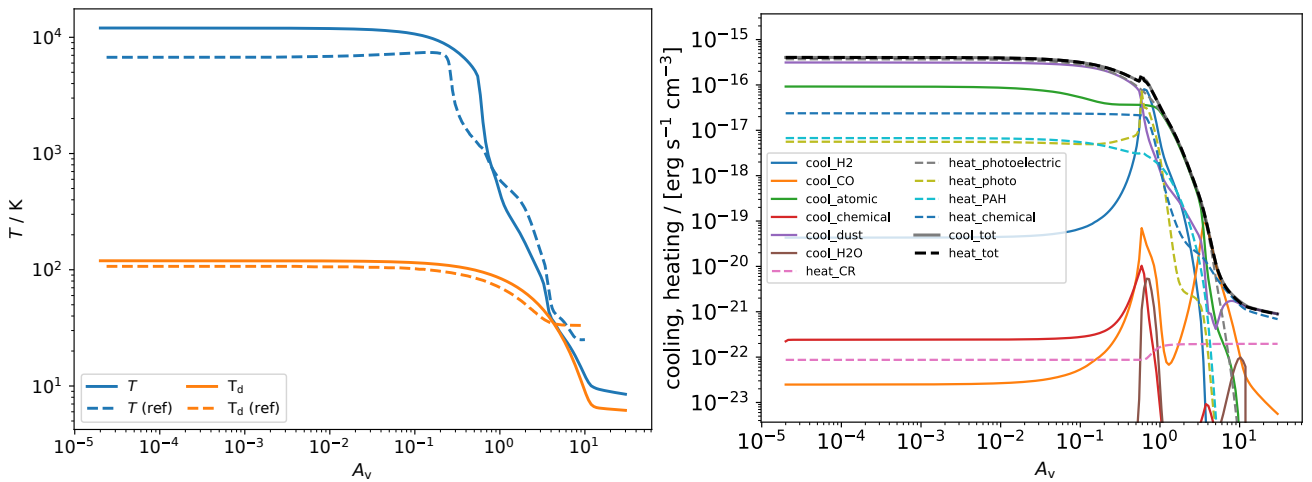


Figure 3. Model V4. **Left panel:** gas (blue) and dust (orange) temperature profiles as a function of the visual extinction A_v . Solid lines are the results from our code, while dashed indicate model “Cloudy” from R07. **Right panel:** cooling (solid) and heating (dashed) functions at different visual extinction values. Grey solid and black dashed lines indicate the sum of the cooling (`cool_tot`) and heating terms (`heat_tot`), respectively.

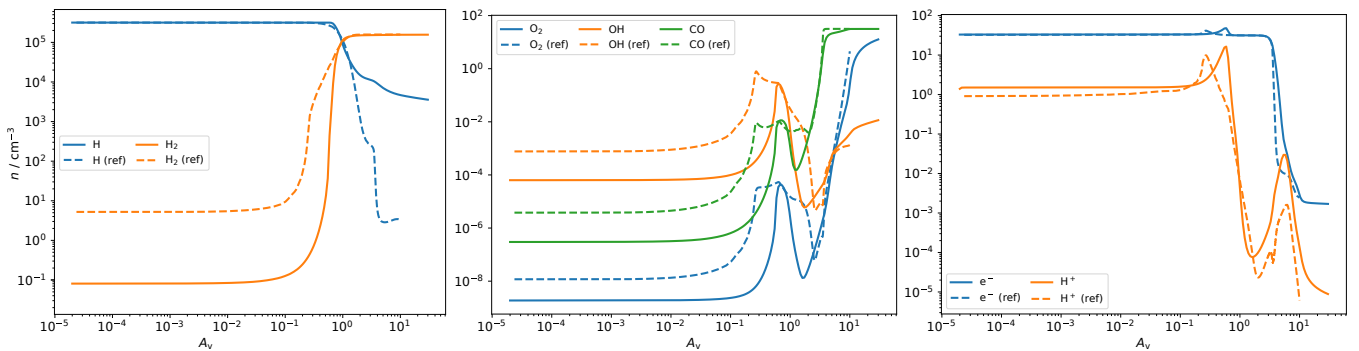


Figure 4. Model V4. **Left panel:** H (blue) and H₂ (orange) density profiles as a function of the visual extinction A_v . Solid lines are the results from our code, while dashed indicate model “Cloudy” from R07. **Middle panel:** O₂ (blue), OH (orange), and CO (green) density profiles as a function of the visual extinction A_v . Solid lines are the results from our code, while dashed indicate model “Cloudy” from R07. **Right panel:** e⁻ (blue) and H⁺ (orange) density profiles as a function of the visual extinction A_v . Solid lines are the results from our code, while dashed indicate model “Cloudy” from R07.

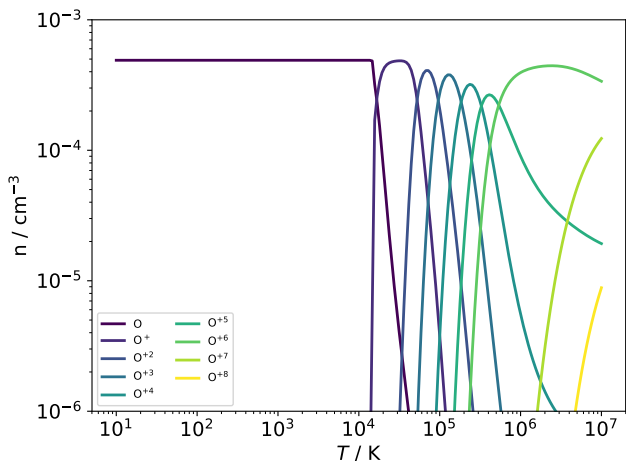


Figure 5. Model Cooling: abundances of oxygen ions at different temperatures assuming equilibrium chemistry.

10^6 yr. The chemical network includes ion-electron recombinations, charge exchange reactions, and collisional ionizations, for all the available atomic ionization levels by using the reactions available in the internal database of PRIZMO (see Sect. 5). Once the chemical equilibrium is reached for all the chemical species (see e.g. oxygen ions in Fig. 5), we evaluate the cooling function, as reported in Fig. 6. We note that `cool_atomic` (i.e. the cooling from collisional excitation lines) dominates at every temperature, except where bremsstrahlung contributes ($T > 5 \times 10^5$ K). Below 10^4 K the cooling is dominated by C and O and their respective ions, as pointed out by Maio et al. (2007) and Gnat & Ferland (2012). The first peak in Fig. 6 is due to hydrogen, and the subsequent peaks are caused by the interplay of carbon and oxygen cooling emission lines, with Ne contributing around 5×10^5 to 10^6 K (cfr. Fig. 3 in Gnat & Ferland 2012).

To ensure that independently from the chemical network the machinery that produces the atomic cooling is working, we verified that the intensity from our emission lines matches the results obtained with CHIANTI¹⁰ for specific temperatures, and protons and electrons densities. Despite some small difference caused by the different chemical network, the results reported in Fig. 6 are similar to what was obtained by Gnat & Ferland (2012), both in term of cooling function and chemical equilibrium¹¹.

4.4 XDR, atomic

To test the effects of a spectrum that includes X-rays we reproduce the set-up from Picogna et al. (2019), where the temperature of a slab of gas is computed for different ionization rates and column densities. In particular, we refer to the dashed black lines in their Fig. 2, where the gas temperature is calculated as a function of the ionization parameter ξ and for three different column densities N . Their results are computed by using the Monte Carlo radiative transfer code MOCASSIN.

¹⁰ <https://github.com/chianti-atomic/ChiantiPy/>

¹¹ <http://wise-obs.tau.ac.il/~orlyg/cooling/CIEion/tab2.txt>

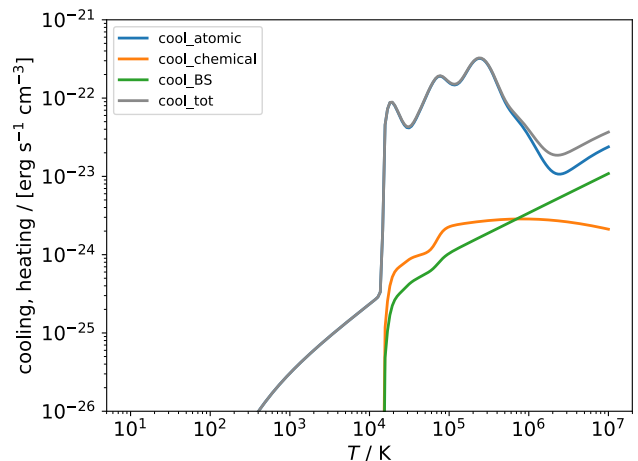


Figure 6. Model Cooling: cooling profile for different temperatures assuming chemical equilibrium. `cool_atomic` (blue solid line) is the collisional radiative cooling, `cool_chemical` (orange) is the cooling from recombination and collisional ionization, `cool_BS` (green) is the bremsstrahlung from ions, and `cool_tot` (grey) is the total cooling.

The ionization parameter is defined as (Tarter et al. 1969; Owen et al. 2010)

$$\xi = \frac{L_x}{nR^2}, \quad (50)$$

where L_x is the X-ray luminosity of the central source, $n = 10^2 \text{ cm}^{-3}$ is the local gas density, and R is the distance from the source.

The set-up is similar to Sect. 4.2, i.e. a semi-infinite slab, with constant density, an emitting source on the left side. However, in this test we only employ atomic species (H, He, C, O, N, S, Si, Ne, and Mg), we have no dust, the line escape probability is disabled (i.e. $\beta = 1$ in Sect. 3.5), and the spectrum (that scales linearly with ξ) is reported in Fig. 7. The reaction rates are chosen using the internal database by following the same criteria as in the cooling test, but extended to the current chemical species. The initial conditions are in Tab. 1. For the present test we adopt a lower limit in temperature of 30 K as in Picogna et al. (2019).

The results obtained in Fig. 8 by PRIZMO are compared to Fig. 2 of Picogna et al. (2019), where three selected column densities are reported, i.e. $N = 5 \times 10^{21}$, $N = 1 \times 10^{22}$, and $N = 2 \times 10^{22} \text{ cm}^{-2}$, computed as $N = nz$, where z is the distance from the left side of the slab, and n is the constant gas density. We note that Picogna et al. (2019) reports a fitting function of the original results from MOCASSIN; these models have a larger variance than the fitting functions, especially in the range $5 \times 10^{-7} \lesssim \xi \lesssim 10^{-5} \text{ erg cm s}^{-1}$. In addition to this, in that interval, the variation of the temperature with N is quite rapid where $5 \times 10^{21} \lesssim N \lesssim 10^{22} \text{ cm}^{-2}$, that explains the discrepancy between the fitting functions from Picogna et al. (2019) and our results around $\xi \approx 10^{-6} \text{ erg cm s}^{-1}$.

To understand what are the dominant thermal processes, we report in Fig. 9 the detailed cooling functions for the model with $\xi = 2 \times 10^{-3} \text{ erg cm s}^{-1}$, where we notice that the chemical cooling from recombination dominates at

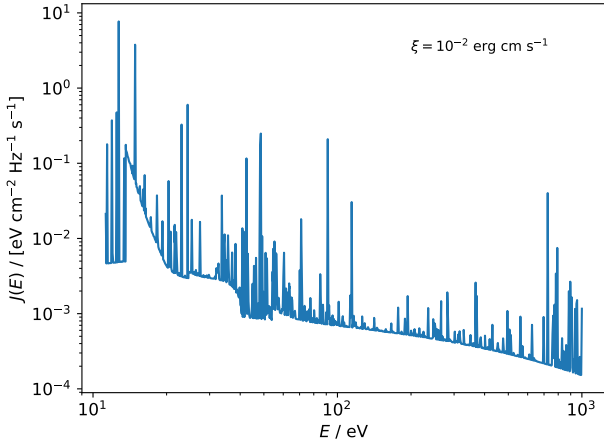


Figure 7. Model XDR, atomic: the radiation spectrum employed for the XDR test as a function of the energy, here reported for $\xi = 2 \times 10^{-3}$ erg cm s $^{-1}$. The spectrum intensity scales linearly with ξ .

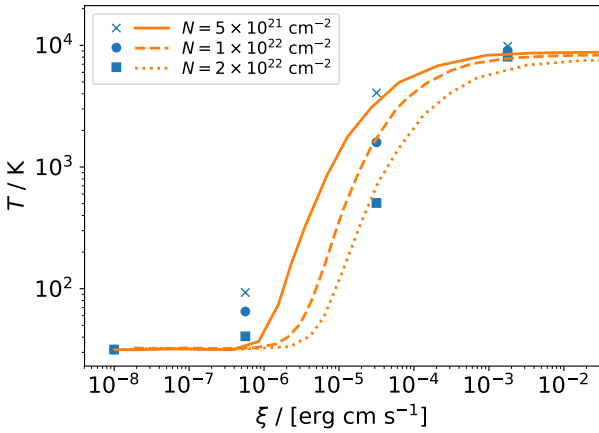


Figure 8. Model XDR, atomic: equilibrium temperature found by our code for different ionization parameter values ξ , at different column densities $N = 5 \times 10^{21}$ cm $^{-2}$ (cross), $N = 1 \times 10^{22}$ cm $^{-2}$ (circle), and $N = 2 \times 10^{22}$ cm $^{-2}$ (square), compared with the fit from Picogna et al. (2019) for the corresponding column densities (respectively solid, dashed, and dotted lines).

lower temperatures, collisional excitation radiative cooling starts to be relevant when $T > 10^4$ K, bremsstrahlung is less important, while heating is dominated by photoionization.

This test shows that PRIZMO produces correct results, similar to what has been obtained by MOCASSIN in Picogna et al. (2019).

5 DATABASES USED BY PRIZMO

PRIZMO requires a large amount of astrochemical data from several sources. For this reason PRIZMO contains an internal database where all the required information is stored and used during the pre-processor stage and at runtime. These

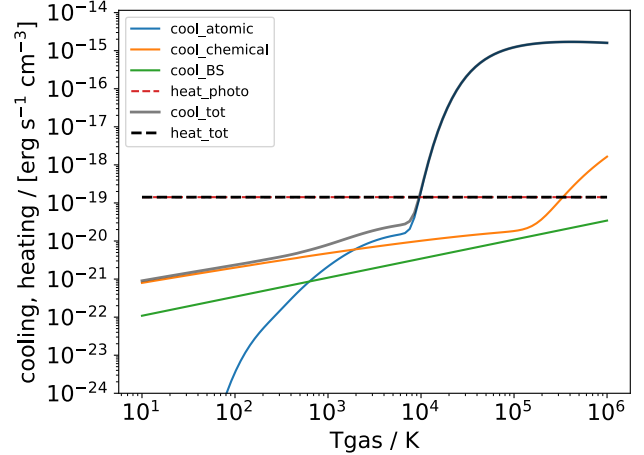


Figure 9. Model XDR, atomic: Cooling function for $\xi = 2 \times 10^{-2}$ erg cm s $^{-1}$ and $N = 5 \times 10^{21}$ cm $^{-2}$, where the individual functions are collisional radiative atomic cooling (solid blue), chemical cooling (solid orange), bremsstrahlung (solid green), and heating from photochemistry (dashed red). Solid grey line is the total cooling. Note that total heating (dashed black) overlaps photoheating.

data are handled by the different PYTHON objects and employed to write parts of the FORTRAN code needed at runtime. For the sake of clarity, we describe in this Section the different databases.

For the collisional atomic line cooling we employ data from KROME and from the CHIANTI database for H, He, Li, Mg, N, C, O, Ne and Si. CHIANTI is the default, unless we have rate collisions from the former, since some of the rates are updated and include additional colliders. We manually inspect the rate coefficients to guarantee that they do not present sharp transitions in temperature, and to extend the range of validity where possible.

Radiative recombination rates are taken from Verner & Ferland (1996), for H-like, He-like, Li-like, and Na-like ions, and from Shull & van Steenberg (1982), Landini & Monsignori Fossi (1990), Landini & Fossi (1991), and Pequignot et al. (1991) for C, N, O, Ne, Na, Al, F, P, Cl, and Fe.

Atomic photoionization cross-sections are taken from Verner & Ferland (1996), where the data is provided as fitting functions of the photon energy.

Charge exchange data are from Arnaud & Rothenflug (1985) for collisions of H $^{(+)}$ and He $^{(+)}$ with Li, C, N, O, Na, Mg $^{(+)}$, Si $^{(+)}$, S, Mn, and Fe $^{(+)}$, while collisional ionizations employ the fit provided by Voronov (1997) for a variety of atoms including H, He, Li, C, N, O, Ne, Na, Mg, Al, Si, S, Cl, Fe, and others less relevant for the current problems.

CO cooling is based on Omukai et al. (2010), and consists of a three-dimensional look-up tables of the local density, the CO column density, and the gas temperature. A similar approach is employed for H $_2$ O. Even if molecular cooling is evaluated by using tables, the code employs data from the LAMDA database to evaluate the molecular lines emission with a machinery similar to the one employed to compute atomic cooling and emissions.

Dust refractive indexes are stored as in Laor & Draine (1993), i.e. with the frequency-dependent real and imaginary parts of the dielectric function for different grain materials.

These data are used to compute the photoelectric heating, and to compute the dust temperature. Dust opacity can be evaluated by the code using the dielectric functions of the grain material and Mie theory¹² (Bohren & Huffman 1983; Giuliano et al. 2019). However, we also include some pre-computed dust opacity tables to reduce the pre-processing time when dust grains have some default material composition (e.g. silicates) and grains size distribution. In this case we employ some of the look-up tables¹³ from Draine (2003), that have also a more complicated treatment including for example PAH.

Apart from specific rate coefficients, e.g. charge exchange, we include the `kida.uva.2014` network from the KIDA database, to include selected rates that are not provided with a FORTRAN expression by the user. However, we note that including reaction rates blindly might cause unpredictable results.

CO self-shielding is taken from Visser et al. (2009) as a function of N_{CO} and N_{H_2} . Although it is possible to retrieve cooling tables for a large set of parameters¹⁴, we limit our data to $b_{\text{CO}} = 0.3 \text{ km s}^{-1}$, $b_{\text{H}_2} = 3 \text{ km s}^{-1}$, $b_{\text{H}} = 5 \text{ km s}^{-1}$, $T_{\text{ex,CO}} = 5 \text{ K}$, $T_{\text{ex,H}_2} = 11.18 \text{ K}$, $[^{12}\text{C}]/[^{13}\text{C}] = 69$, $[^{16}\text{O}]/[^{18}\text{O}] = 557$, and $[^{18}\text{O}]/[^{17}\text{O}] = 3.6$. For N_2 self-shielding we follow an analogous by using the tables¹⁴ from Heays et al. (2014), with $b_{\text{N}_2} = 0.17 \text{ km s}^{-1}$, $b_{\text{H}_2} = 3 \text{ km s}^{-1}$, $b_{\text{H}} = 5 \text{ km s}^{-1}$, $T_{\text{ex},^{14}\text{N}_2} = T_{\text{ex},^{14}\text{N}^{15}\text{N}} = T_{\text{ex,H}_2} = 50 \text{ K}$, and $[^{14}\text{N}_2]/[^{14}\text{N}^{15}\text{N}] = 225$.

Thermochemical data are taken from Burcat’s polynomials, that are functions of the temperature. For each species these consist of two individual polynomials for two different contiguous temperature ranges. These a_i coefficients can be employed to compute the enthalpy of formation using

$$\frac{\Delta H_f^\circ(T)}{RT} = \sum_{i=1}^5 \frac{a_i T^{i-1}}{i} + \frac{a_6}{T}, \quad (51)$$

where R is the gas constant.

Energy-dependent molecular cross-sections for photoionization and photodissociation reactions are taken from the LEIDEN database¹⁴ and limited to the branching ratios indicated there. We do employ the version of the database that instead of using specific lines has a regular grid spacing of 0.1 nm, where the area of the cross-section in each bin is equivalent to the area of the sum of the cross-sections of the lines within that bin. PRIZMO can use the cross-sections from the database but with different branching ratios, using a specific decorator in the chemical network file (see Appendix A).

For X-ray reactions with molecules we need the partial cross-sections for the different atomic shells, and the list of cross-sections needed to compute the total cross-sections of a given reaction, so that for example $\text{CO} \rightarrow \text{C}^+ + \text{O}^+ + 2e^-$ has $\sigma_{\text{CO}} = 0.5(\sigma_{\text{C,K}} + \sigma_{\text{C,L}} + \sigma_{\text{O,K}} + \sigma_{\text{O,L}})$, where the first subscript is the atomic species, while the second indicates the shell. These data are taken from Ádámkóvics et al. (2011) and collected with the advice of C. Rab (private comm.); see Appendix I.

6 LIMITATIONS

PRIZMO presents a set of limitations due to the fact that many microphysical processes are required to model gas and dust in a protoplanetary disk, and which can span a large range of temperatures, densities, and radiation spectra (see e.g. Haworth et al. 2016). There are three types of approximations: (i) the limited knowledge of the physics and the chemistry in disks, for example some of the reaction rate coefficients are available only within small temperature ranges, and their extrapolation outside the interval is arbitrary. (ii) The simplification required to model complicated physical processes that are tightly interconnected, or that present a large number of parameters and variables. Finally, (iii) solving time-dependent chemistry and microphysics coupled with multi-frequency radiative transfer, or with hydrodynamics, presents a demanding computational challenge, and for this reason we are forced to simplify the description even of some processes with well-understood mechanisms, but with a large numerical footprint, in order to make these simulations feasible.

We will not discuss the problems related to the physical/chemical uncertainties, since they have been already discussed in the previous sections, but we will explain the caveats and the limitations related to our specific implementation. However, processes that are currently simplified might be improved in the future, thanks to the development of numerical techniques, dedicated hardware, and a better understanding of chemistry, microphysics, and protoplanetary disks.

A consistent limitation of our model is the problem of dealing with multi-frequency radiation, and includes not only FUV, but also X-rays. Unfortunately, it is very demanding to model radiation transport with an energy binning that matches exactly the features a large number of molecular and atomic cross-sections, and so we must instead limit our methodology to a reduced spectrum. This limitation might over or underestimate the photochemical rate coefficients (see Paper I), affecting the chemical and (consequently) the thermal evolution.

Analogously, some of the key reactions that require the knowledge of the intensity of the radiation in several energy bins are treated with a reduced method, that is based on pre-computed radiation with some specific spectral shape, e.g. the Draine radiation field. Computing the equivalent integrated intensity in a specific band is clearly a limitation, since the effects due to “non-Draine” shapes are completely lost. This limitation applies to H_2 and CO photodissociation. Similarly, using pre-computed methods for self-shielding of the same molecules, reduces the capability of modelling the thermochemistry of a disk consistently.

Although PRIZMO’s capability to compute the emission from the chemical species included in the network, we assume that the radiation produced is lost, and therefore does not feedback on the resulting radiation spectra that come out of the simulated cell, i.e. after being attenuated by dust and photochemical reactions. This is because we do not compute the shape of the lines that are emitted, but in principle this limitation might be overcome in the future.

Another limit comes from the (currently) fixed grain size distribution. Although, this constraint allows the code to pre-compute a large set of quantities that save consid-

¹² See e.g. <http://scatterlib.wikidot.com/mie> and https://bitbucket.org/tgrassi/compute_qabs/.

¹³ <https://www.astro.princeton.edu/~draine/>

¹⁴ <https://home.strw.leidenuniv.nl/~ewine/photo>

erable computational resources at runtime, the size distribution of dust grains can vary drastically over the extent and lifetime of a disk (Testi et al. 2014), so that this approach might lead to misleading results, in particular when surface chemistry is dominant. This also strongly affects the gas temperature (e.g. when dust cooling dominates). In order to enable this functionality in the future, PRIZMO would need to be coupled with a dedicated code for dust evolution (e.g. Birnstiel et al. 2012).

A similar discussion applies to cosmic rays, which are treated with a single parameter, i.e. the ionization rate. In principle, their propagation is related to the geometry of the disk (Bai & Goodman 2009; Cleeves et al. 2013) and to the topology of the magnetic fields (Padovani et al. 2014), suggesting that, to find the proper ionization rate, we need a non-local treatment, and for this reason this might result in over/underestimating their heating, and their effect on the chemistry, especially where the radiation does not play the main role. Additionally, we do not include any cosmic rays-induced fluorescence, that might have relevant effects on the charge of grains (Ivlev et al. 2015) and on the gas chemistry (Visser et al. 2018).

7 SUMMARY

We present PRIZMO, a code for evolving thermochemistry in protoplanetary disks, capable of being coupled with hydrodynamical and multifrequency radiative transfer codes. We discussed the main features of the code, including gas and surface chemistry, photochemistry, and the main cooling and heating processes. We also reported how we tackled different computational bottlenecks, and what are the main algorithms employed. To prove the validity of the results obtained by PRIZMO, we presented a set of benchmarks that include photon-dominated regions, slabs illuminated by radiation that include X-ray, and well-established cooling functions evaluated at different temperatures. These tests shows an agreement with the benchmarks both in terms of chemical and thermal structures.

This work represents the first step to provide a tool to explore the thermochemical properties of the wind launching region of protoplanetary disks and to determine the observational features from molecular tracers entrapped in the photoevaporative wind. This specific topic will be discussed in a forthcoming paper where we will show the results obtained by coupling PRIZMO with a Monte Carlo radiative transfer code (MOCASSIN), and then with a hydrodynamical code (PLUTO, Mignone et al. 2007).

ACKNOWLEDGEMENTS

We acknowledge J. P. Ramsey, C. Rab, M. Ádámkóvics, and the referee for useful comments and discussions. TG acknowledges C. Clarke for the hospitality during his visit at the IoA in Cambridge in the Framework of the Cambridge-LMU Strategic partnership Grant. GP acknowledges support from the DFG Research Unit FOR 2634/1, ER 685/8-1. LSz acknowledges support from the DFG Research Unit FOR 2634/1, CA 1624/1-1. BE acknowledges support from the DFG cluster of excellence “Origin and Structure of

the Universe” (<http://www.universe-cluster.de/>). This work was funded by the DFG Research Unit FOR 2634/1 ER685/11-1.

REFERENCES

- Ádámkóvics M., Glassgold A. E., Meijerink R., 2011, *ApJ*, **736**, 143
- Akimkin V., Zhukovska S., Wiebe D., Semenov D., Pavlyuchenkov Y., Vasyunin A., Birnstiel T., Henning T., 2013, *ApJ*, **766**, 8
- Alexander R. D., 2008, *MNRAS*, **391**, L64
- Alexander R. D., Pascucci I., 2012, *MNRAS*, **422**, L82
- Alexander R. D., Clarke C. J., Pringle J. E., 2006a, *MNRAS*, **369**, 216
- Alexander R. D., Clarke C. J., Pringle J. E., 2006b, *MNRAS*, **369**, 229
- Alexander R., Pascucci I., Andrews S., Armitage P., Cieza L., 2014, in Beuther H., Klessen R. S., Dullemond C. P., Henning T., eds, *Protostars and Planets VI*. p. 475 ([arXiv:1311.1819](https://arxiv.org/abs/1311.1819)), doi:10.2458/azu_uapress_9780816531240-ch021
- Andersson S., van Dishoeck E. F., 2008, *A&A*, **491**, 907
- Armitage P. J., 2011, *ARA&A*, **49**, 195
- Arnaud M., Rothenflug R., 1985, *A&AS*, **60**, 425
- Bai X.-N., 2011, *ApJ*, **739**, 50
- Bai X.-N., Goodman J., 2009, *ApJ*, **701**, 737
- Bakes E. L. O., Tielens A. G. G. M., 1994, *ApJ*, **427**, 822
- Banzatti A., Pascucci I., Edwards S., Fang M., Gorti U., Flock M., 2019, *ApJ*, **870**, 76
- Birnstiel T., Klahr H., Ercolano B., 2012, *A&A*, **539**, A148
- Bisbas T. G., Haworth T. J., Barlow M. J., Viti S., Harries T. J., Bell T., Yates J. A., 2015, *MNRAS*, **454**, 2828
- Bohren C. F., Huffman D. R., 1983, *Absorption and scattering of light by small particles*. Wiley
- Booth R. A., Ilee J. D., 2019, *MNRAS*, **487**, 3998
- Bruderer S., Doty S. D., Benz A. O., 2009, *ApJS*, **183**, 179
- Burcat A., 1984, in Gardiner W. C. J., ed., *Combustion Chemistry*. Springer US, pp 455–473, doi:10.1007/978-1-4684-0186-8_8
- Carrera D., Ford E. B., Izidoro A., Jontof-Hutter D., Raymond S. N., Wolfgang A., 2018, *ApJ*, **866**, 104
- Cazaux S., Spaans M., 2009, *A&A*, **496**, 365
- Cazaux S., Minissale M., Dulieu F., Hocuk S., 2016, *A&A*, **585**, A55
- Cen R., 1992, *ApJS*, **78**, 341
- Cleeves L. I., Adams F. C., Bergin E. A., 2013, *ApJ*, **772**, 5
- Cuppen H. M., Walsh C., Lamberts T., Semenov D., Garrod R. T., Penteado E. M., Ioppolo S., 2017, *Space Sci. Rev.*, **212**, 1
- Draine B. T., 1978, *ApJS*, **36**, 595
- Draine B. T., 2003, *ApJ*, **598**, 1026
- Draine B. T., 2009, in Henning T., Grün E., Steinacker J., eds, *Astronomical Society of the Pacific Conference Series Vol. 414, Cosmic Dust - Near and Far*. p. 453 ([arXiv:0903.1658](https://arxiv.org/abs/0903.1658))
- Draine B. T., 2011, *Physics of the Interstellar and Intergalactic Medium*. Princeton University Press
- Draine B. T., Bertoldi F., 1996, *ApJ*, **468**, 269
- Draine B. T., Sutin B., 1987, *ApJ*, **320**, 803
- Drążkowska J., Alibert Y., Moore B., 2016, *A&A*, **594**, A105
- Ercolano B., Owen J. E., 2010, *MNRAS*, **406**, 1553
- Ercolano B., Owen J. E., 2016, *MNRAS*, **460**, 3472
- Ercolano B., Pascucci I., 2017, *Royal Society Open Science*, **4**, 170114
- Ercolano B., Rosotti G., 2015, *MNRAS*, **450**, 3008
- Ercolano B., Barlow M. J., Storey P. J., Liu X. W., 2003, *MNRAS*, **340**, 1136
- Ercolano B., Barlow M. J., Storey P. J., 2005, *MNRAS*, **362**, 1038

- Ercolano B., Weber M. L., Owen J. E., 2018, *MNRAS*, **473**, L64
- Fujii Y. I., Okuzumi S., Inutsuka S.-I., 2011, *ApJ*, **743**, 53
- Galli D., Padovani M., 2015, [arXiv:1502.03380](https://arxiv.org/abs/1502.03380),
- Giuliano B. M., et al., 2019, *A&A*, **629**, A112
- Glassgold A. E., Najita J. R., Igea J., 2007, *ApJ*, **656**, 515
- Glover S., 2015, preprint, ([arXiv:1501.05960](https://arxiv.org/abs/1501.05960))
- Glover S. C. O., Abel T., 2008, *MNRAS*, **388**, 1627
- Gnat O., Ferland G. J., 2012, *ApJS*, **199**, 20
- Grassi T., Bovino S., Schleicher D. R. G., Prieto J., Seifried D., Simoncini E., Gianturco F. A., 2014, *MNRAS*, **439**, 2386
- Grassi T., Bovino S., Haugbølle T., Schleicher D. R. G., 2017, *MNRAS*, **466**, 1259
- Grassi T., Padovani M., Ramsey J. P., Galli D., Vaytet N., Ercolano B., Haugbølle T., 2019, *MNRAS*, **484**, 161
- Hasegawa T. I., Herbst E., 1993, *MNRAS*, **261**, 83
- Haworth T. J., et al., 2016, *PASA*, **33**, e053
- Heays A. N., Visser R., Gredel R., Ubachs W., Lewis B. R., Gibson S. T., van Dishoeck E. F., 2014, *A&A*, **562**, A61
- Heays A. N., Bosman A. D., van Dishoeck E. F., 2017, *A&A*, **602**, A105
- Hindmarsh A. C., Brown P. N., Grant K. E., Lee S. L., Serban R., Shumaker D. E., Woodward C. S., 2005, *ACM Trans. Math. Softw.*, **31**, 363
- Hocuk S., Cazaux S., 2015, *A&A*, **576**, A49
- Hocuk S., Szűcs L., Caselli P., Cazaux S., Spaans M., Esplugues G. B., 2017, *A&A*, **604**, A58
- Hollenbach D., McKee C. F., 1979, *ApJS*, **41**, 555
- Hollenbach D., Kaufman M. J., Bergin E. A., Melnick G. J., 2009, *ApJ*, **690**, 1497
- Ilee J. D., et al., 2017, *MNRAS*, **472**, 189
- Ilgner M., Nelson R. P., 2006, *A&A*, **445**, 205
- Ivlev A. V., Padovani M., Galli D., Caselli P., 2015, *ApJ*, **812**, 135
- Jennings J., Ercolano B., Rosotti G. P., 2018, *MNRAS*, **477**, 4131
- Kunitomo M., Suzuki T. K., Inutsuka S.-i., 2020, arXiv e-prints, p. [arXiv:2001.03949](https://arxiv.org/abs/2001.03949)
- Landini M., Fossi B. C. M., 1991, *A&AS*, **91**, 183
- Landini M., Monsignori Fossi B. C., 1990, *A&AS*, **82**, 229
- Laor A., Draine B. T., 1993, *ApJ*, **402**, 441
- Leger A., Jura M., Omont A., 1985, *A&A*, **144**, 147
- Leitch-Devlin M. A., Williams D. A., 1985, *MNRAS*, **213**, 295
- Li A., Draine B. T., 2000, arXiv e-prints, pp astro-ph/0012509
- Maior U., Dolag K., Ciardi B., Tornatore L., 2007, *MNRAS*, **379**, 963
- Mathis J. S., Rumpl W., Nordsieck K. H., 1977, *ApJ*, **217**, 425
- McElroy D., Walsh C., Markwick A. J., Cordiner M. A., Smith K., Millar T. J., 2013, *A&A*, **550**, A36
- Mignone A., Bodo G., Massaglia S., Matsakos T., Tesileanu O., Zanni C., Ferrari A., 2007, *ApJS*, **170**, 228
- Minissale M., Dulieu F., Cazaux S., Hocuk S., 2016, *A&A*, **585**, A24
- Natta A., Testi L., Alcalá J. M., Rigliaco E., Covino E., Stelzer B., D'Elia V., 2014, *A&A*, **569**, A5
- Neufeld D. A., Kaufman M. J., 1993, *ApJ*, **418**, 263
- Nishi R., Nakano T., Umebayashi T., 1991, *ApJ*, **368**, 181
- Okuzumi S., 2009, *ApJ*, **698**, 1122
- Omukai K., Hosokawa T., Yoshida N., 2010, *ApJ*, **722**, 1793
- Owen J. E., Ercolano B., Clarke C. J., Alexander R. D., 2010, *MNRAS*, **401**, 1415
- Owen J. E., Ercolano B., Clarke C. J., 2011, *MNRAS*, **412**, 13
- Owen J. E., Clarke C. J., Ercolano B., 2012, *MNRAS*, **422**, 1880
- Padovani M., Galli D., Hennebelle P., Commerçon B., Joos M., 2014, *A&A*, **571**, A33
- Pascucci I., Sterzik M., 2009, *ApJ*, **702**, 724
- Penteado E. M., Walsh C., Cuppen H. M., 2017, *ApJ*, **844**, 71
- Pequignot D., Petitjean P., Boisson C., 1991, *A&A*, **251**, 680
- Picogna G., Ercolano B., Owen J. E., Weber M. L., 2019, *MNRAS*, **487**, 691
- Richings A. J., Schaye J., Oppenheimer B. D., 2014, *MNRAS*, **442**, 2780
- Rigliaco E., Pascucci I., Gorti U., Edwards S., Hollenbach D., 2013, *ApJ*, **772**, 60
- Rodenkirch P. J., Klahr H., Fendt C., Dullemond C. P., 2020, *A&A*, **633**, A21
- Röllig M., et al., 2007, *A&A*, **467**, 187
- Ruaud M., Wakelam V., Hersant F., 2016, *MNRAS*, **459**, 3756
- Schisano E., Ercolano B., Güdel M., 2010, *MNRAS*, **401**, 1636
- Schöier F. L., van der Tak F. F. S., van Dishoeck E. F., Black J. H., 2005, *A&A*, **432**, 369
- Semenov D., et al., 2010, *A&A*, **522**, A42
- Shull J. M., van Steenberg M., 1982, *ApJS*, **48**, 95
- Simon M. N., Pascucci I., Edwards S., Feng W., Gorti U., Hollenbach D., Rigliaco E., Keane J. T., 2016, *ApJ*, **831**, 169
- Stahler S. W., Shu F. H., Taam R. E., 1981, *ApJ*, **248**, 727
- Sutherland R. S., Dopita M. A., 1993, *ApJS*, **88**, 253
- Tarter C. B., Tucker W. H., Salpeter E. E., 1969, *ApJ*, **156**, 943
- Testi L., et al., 2014, *Protostars and Planets VI*, pp 339–361
- Throop H. B., Bally J., 2005, *ApJ*, **623**, L149
- Tielens A. G. G. M., 2010, *The Physics and Chemistry of the Interstellar Medium*. Cambridge University Press
- Verner D. A., Ferland G. J., 1996, *ApJS*, **103**, 467
- Visser R., van Dishoeck E. F., Black J. H., 2009, *A&A*, **503**, 323
- Visser R., Bruderer S., Cazzoletti P., Facchini S., Heays A. N., van Dishoeck E. F., 2018, *A&A*, **615**, A75
- Voronov G. S., 1997, *Atomic Data and Nuclear Data Tables*, **65**, 1
- Wakelam V., et al., 2012, *ApJS*, **199**, 21
- Wakelam V., et al., 2017, *Molecular Astrophysics*, **9**, 1
- Wang L., Goodman J., 2017, *ApJ*, **847**, 11
- Weingartner J. C., Draine B. T., 2001, *ApJ*, **548**, 296
- Weingartner J. C., Draine B. T., Barr D. K., 2006, *ApJ*, **645**, 1188
- Woitke P., Kamp I., Thi W.-F., 2009, *A&A*, **501**, 383
- Xu Y., McCray R., 1991, *ApJ*, **375**, 190

APPENDIX A: REACTION RATES FORMAT

Here we report examples of the possible expressions that can be employed to represent chemical reactions in PRIZMO.

To indicate a custom expression for the rate in the temperature range from zero to 6700 K we use for example

```
H + H+ -> H2+ [ ,6700] 1.85d-23*Tgas**1.8
```

where the reaction rate is written using standard FORTRAN syntax, but it can also be written as

```
H + H+ -> H2+ [ ] KIDA
```

that employs the corresponding rate from the KIDA database internally stored (including temperature limits), i.e. the `kida.uva.2014` version.

Analogously, special reactions not present in KIDA will be defined by special expression as

```
C++ + E -> C+ [ ] RECOMBINATION
```

or

```
C [ ,4] ALL_RECOMBINATION
```

if the user wants to include all the recombination rates of carbon ions up to the fourth ionization level. In this case reactions are taken from the internal database of recombination rates. A detailed description of the databases employed can be found in Sect. 5.

Photochemical rates can be defined with


```
C -> C+ + E [ ] PHOTO
```

so that PRIZMO will select the correct cross-section from the database. For molecular chemical reactions without branching ratio specification, or with only a branching ratio, it is possible to indicate this by using a JSON structure as follows

```
H3+ -> H2+ + H [ ]PHOTO {"branching_ratio": 0.5}
H3+ -> H2 + H+ [ ]PHOTO {"branching_ratio": 0.5}
```

where the cross-section for H_3^+ is taken from the LEIDEN database, but the branching ratios are defined by the user.

Chemistry on grains can be defined by using

```
CO_dust -> CO [ ]
CO -> CO_dust [ ]
C_dust + O_dust -> CO_dust [ ]
```

which will result in the pre-processor using the conventions defined in Sect. 2.3. Binding energies and activation barrier values can be overridden with a JSON data structure similar to defining the branching ratios above.

The code recognises certain decorators for special actions, e.g. to select a subset of reactions by using `@include_only_species:H, CO, CH, C2`, that selects all the reactions that includes these specific species. Analogously, blocks can be defined using a C-like format to indicate special reactions to the PYTHON preprocessor, for example

```
block_evaluate_once{
  block_cosmic_rays{
    H2 -> H+ + H + E [ ]0.02e+00 * variable_crflux
    H2 -> H + H [ ]0.10e+00 * variable_crflux
  }
}
```

to use these reactions for the cosmic-rays heating, and to force the code to evaluate these rates only once (see Sect. 2.6).

APPENDIX B: DISCRETIZATION OF INTEGRALS TO TAKE ADVANTAGE OF VECTORIZATION

The integrals that are based on variable quantities are written in order to have a vector of pre-computed constants multiplied by the vector with the variables. An example is a photochemical rate, where the radiation flux $J(E)$ is variable, while the rest of the integral can be pre-determined as in

$$k = \int_{E_{\text{th}}}^{E_{\text{max}}} \frac{\sigma(E)J(E)}{E} dE, \quad (\text{B1})$$

that can be written as

$$k = \int_{E_{\text{th}}}^{E_{\text{max}}} A(E)dE, \quad (\text{B2})$$

and discretized using the trapezoidal rule in N unequally-spaced energy grid points as

$$k = \frac{1}{2} \sum_{i=2}^N (A_{i-1} + A_i) (E_i - E_{i-1}). \quad (\text{B3})$$

The corresponding expanded expression using some algebra and grouping the terms by A_i becomes

$$2k = A_1(E_2 - E_1) + \sum_{i=2}^{N-1} A_i(E_{i+1} - E_{i-1}) + A_N(E_N - E_{N-1}) \quad (\text{B4})$$

that using the definition of A_i becomes

$$2k = \sum_{i=1}^N J_i \frac{\sigma_i x_i}{E_i}, \quad (\text{B5})$$

where

$$x_1 = E_2 - E_1 \quad (\text{B6})$$

$$x_i = E_{i+1} - E_{i-1} \quad (\text{B7})$$

$$x_N = E_N - E_{N-1}. \quad (\text{B8})$$

Eq. (B5) is then

$$2k = \sum_{i=1}^N J_i B_i, \quad (\text{B9})$$

where J_i is a vector that changes at runtime, while B_i can be pre-calculated. PRIZMO takes advantage from this pre-calculation and from the fact that the expression can be easily vectorized as `k=0.5*sum(J(:)*B(:))` using the FORTRAN syntax.

APPENDIX C: ANALYTICAL SOLUTION OF A LINEAR SYSTEM WITH A SUPERDIAGONAL COEFFICIENTS MATRIX AND CONSERVATION

The code frequently tries to find the solution of a linear system $A \times x = b$ with N unknowns, and a matrix A of the form $A_{ij} = 0$, except $A_{ii} \neq 0$, $A_{i,i+1} \neq 0$, and $A_{Ni} = 1$, and $b_i = 0$, except $b_N \neq 0$. The last row of A represents conservation (i.e. $\sum_i x_i = b_N$), and apart from this row, the rest of the matrix is superdiagonal. This can be solved by defining $w_2 = A_{11}/A_{12}$ and $w_i = w_{i-1}A_{i-1,i-1}/A_{i-1,i}$ for $3 \leq i \leq N$, the unknowns are then $x_1 = b_N/(1 + \sum_{i=2}^N w_i)$ and $x_i = w_i/x_1$ for $i > 1$. Solving the matrix analytically instead of using e.g. `dgesv` from LAPACK reduces considerably the computational time.

APPENDIX D: MOLECULAR HYDROGEN COOLING TABLES (LOW DENSITY LIMIT)

We report the functions employed for the low density limit of the molecular hydrogen cooling (Glover & Abel 2008; Grassi et al. 2014; Glover 2015), where $\Lambda_{\text{H}_2}^{\text{low}} = \Lambda_{\text{H}_2,\text{H}}^{\text{low}} + \Lambda_{\text{H}_2,\text{H}^+}^{\text{low}} + \Lambda_{\text{H}_2,\text{H}_2}^{\text{low}} + \Lambda_{\text{H}_2,\text{e}^-}^{\text{low}} + \Lambda_{\text{H}_2,\text{He}}^{\text{low}}$.

H₂-H

If $T \leq 10^2$ K

$$\begin{aligned} \Lambda_{\text{H}_2,\text{H}}^{\text{low}} &= \text{dex}(-16.818342 + 37.383713t_3 \\ &+ 58.145166t_3^2 + 48.656103t_3^3 \\ &+ 20.159831t_3^4 + 3.8479610t_3^5) n_{\text{H}}, \quad (\text{D1}) \end{aligned}$$

if $10^2 < T \leq 10^3$ K

$$\begin{aligned} \Lambda_{\text{H}_2, \text{H}}^{\text{low}} &= \text{dex}(-24.311209 + 3.5692468t_3 \\ &\quad - 11.332860t_3^2 - 27.850082t_3^3 \\ &\quad - 21.328264t_3^4 + 4.2519023t_3^5) n_{\text{H}}, \end{aligned} \quad (\text{D2})$$

if $10^3 < T \leq 6 \times 10^3$ K

$$\begin{aligned} \Lambda_{\text{H}_2, \text{H}}^{\text{low}} &= \text{dex}(-24.311209 + 4.6450521t_3 \\ &\quad - 3.7209846t_3^2 + 5.9369081t_3^3 \\ &\quad - 5.5108049t_3^4 + 1.5538288t_3^5) n_{\text{H}}, \end{aligned} \quad (\text{D3})$$

and if $T > 6 \times 10^3$ K

$$\Lambda_{\text{H}_2, \text{H}}^{\text{low}} = 1.8623 \times 10^{-22} w(T) n_{\text{H}}, \quad (\text{D4})$$

where $\text{dex}(x) = 10^x$, and $t_3 = \log(T/10^3 \text{ K})$.

H₂-H⁺

If $10 < T \leq 10^4$ K

$$\begin{aligned} \Lambda_{\text{H}_2, \text{H}^+}^{\text{low}} &= \text{dex}(-22.089523 + 1.5714711t_3 \\ &\quad + 0.015391166t_3^2 - 0.23619985t_3^3 \\ &\quad - 0.51002221t_3^4 + 0.32168730t_3^5) n_{\text{H}^+}, \end{aligned} \quad (\text{D5})$$

and if $T > 10^4$ K

$$\Lambda_{\text{H}_2, \text{H}^+}^{\text{low}} = 1.18250913 \times 10^{-21} w(T) n_{\text{H}^+}. \quad (\text{D6})$$

H₂-H₂

If $10^2 < T \leq 10^4$ K

$$\begin{aligned} \Lambda_{\text{H}_2, \text{H}_2}^{\text{low}} &= \text{dex}(-23.962112 + 2.09433740t_3 \\ &\quad + 0.77151436t_3^2 + 0.43693353t_3^3 \\ &\quad - 0.14913216t_3^4 - 0.033638326t_3^5) \\ &\quad \cdot w(x) n_{\text{H}_2}. \end{aligned} \quad (\text{D7})$$

for which we assume ortho-to-para ratio of 3:1.

H₂-e⁻

If $T \leq 5 \times 10^2$ K

$$\begin{aligned} \Lambda_{\text{H}_2, \text{e}^-}^{\text{low}} &= \text{dex}(-2.1928796 + 16.815730t_3 \\ &\quad + 96.743155t_3^2 + 343.19180t_3^3 \\ &\quad + 734.71651t_3^4 + 983.67576t_3^5 \\ &\quad + 801.81247t_3^6 + 364.14446t_3^7 \\ &\quad + 70.609154t_3^8) n_{\text{e}^-}, \end{aligned} \quad (\text{D8})$$

if $T > 5 \times 10^2$ K

$$\begin{aligned} \Lambda_{\text{H}_2, \text{e}^-}^{\text{low}} &= \text{dex}(-22.921189 + 1.6815730t_3 \\ &\quad + 0.9331062t_3^2 + 4.0406627t_3^3 \\ &\quad - 4.7274036t_3^4 - 8.8077017t_3^5 \\ &\quad + 8.9167183t_3^6 + 6.4380698t_3^7 \\ &\quad - 6.3701156t_3^8) w(T) n_{\text{e}^-}, \end{aligned} \quad (\text{D9})$$

H₂-He

If $10 < T \leq 5 \times 10^4$ K

$$\begin{aligned} \Lambda_{\text{H}_2, \text{He}}^{\text{low}} &= \text{dex}(-23.689237 + 2.1892372t_3 \\ &\quad - 0.8152044t_3^2 + 0.2903628t_3^3 \\ &\quad - 0.1659618t_3^4 + 0.1919138t_3^5) n_{\text{He}}, \end{aligned} \quad (\text{D10})$$

otherwise

$$\Lambda_{\text{H}_2, \text{He}}^{\text{low}} = 1.0025604 \times 10^{-22} w(T) n_{\text{He}}. \quad (\text{D11})$$

APPENDIX E: MOLECULAR HYDROGEN HIGH-DENSITY LIMIT

If $T < 2 \times 10^3$ K, the rotational high density cooling function is

$$\begin{aligned} \Lambda_{\text{H}_2, \text{R}}^{\text{high}} &= \frac{9.5 \times 10^{-22} t_3^{3.76}}{1 + 0.12 t_3^{2.1}} \exp\left[\left(-\frac{0.13}{T_3}\right)^3\right] \\ &\quad + 3 \times 10^{-24} \exp\left(-\frac{0.51}{T_3}\right), \end{aligned} \quad (\text{E1})$$

with $T_3 = T/10^3$ K, while the vibrational cooling function is

$$\begin{aligned} \Lambda_{\text{H}_2, \text{V}}^{\text{high}} &= 6.7 \times 10^{-19} \exp\left(\frac{-5.86}{T_3}\right) \\ &\quad + 1.6 \times 10^{-18} \exp\left(\frac{-11.7}{T_3}\right), \end{aligned} \quad (\text{E2})$$

so that the total high density is $\Lambda_{\text{H}_2}^{\text{high}} = \Lambda_{\text{H}_2, \text{R}}^{\text{high}} + \Lambda_{\text{H}_2, \text{V}}^{\text{high}}$, while if $2 \times 10^3 \leq T < 10^4$ K

$$\begin{aligned} \Lambda_{\text{H}_2}^{\text{high}} &= \text{dex}(-20.584225 + 5.0194035t_3 \\ &\quad - 1.5738805t_3^2 - 4.7155769t_3^3 \\ &\quad + 2.4714161t_3^4 + 5.4710750t_3^5 \\ &\quad - 3.9467356t_3^6 - 2.2148338t_3^7 \\ &\quad + 1.8161874t_3^8), \end{aligned} \quad (\text{E3})$$

otherwise

$$\Lambda_{\text{H}_2}^{\text{high}} = \frac{5.53133 \times 10^{-19}}{1 + \exp[0.0002(T - 3 \times 10^4 \text{ K})]}. \quad (\text{E4})$$

APPENDIX F: H₂ FORMATION ON DUST GRAINS (BENCHMARK V1 AND V4)

The impact of molecular hydrogen formation has a relevant impact on the results obtained in benchmark **V1** and **V4**. In Fig. **F1** for the two benchmarks we report the rate coefficient in Eq. (12) (labelled C09) compared with the expression from R07 we employed in the tests, i.e. $k_{\text{d}} = 3 \times 10^{-18} \sqrt{T_{\text{d}}} \text{ cm}^3 \text{ s}^{-1}$. While in **V1** the rate coefficients are similar, the higher gas temperature of **V4** affects the sticking in Eq. (5), causing a much lower molecular hydrogen formation efficiency. Following these results, since we are more interested in benchmarking the photochemical part of the code, we employ the expression from R07 in the benchmarks in Sect. 4 instead of Eq. (12).

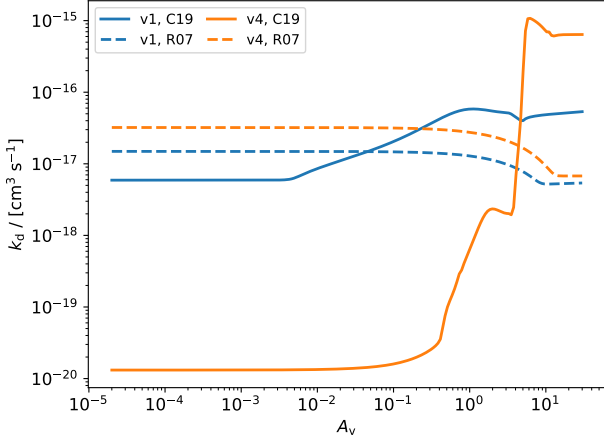


Figure F1. Comparison of the rate coefficients of molecular hydrogen formation on dust grains as a function of visual extinction for the models V1 (blue lines) and V4 (orange lines). The solid lines labelled C09 employ the model from [Cazaux & Spaans \(2009\)](#) in Eq. (12), while the dashed lines labelled R07 use [Röllig et al. \(2007\)](#).

APPENDIX G: CHEMICAL NETWORK (TESTS V1 AND V4)

We report the chemical network employed for the R07 benchmark tests in Tab. G1, Tab. G2, and Tab. G3.

1	H + CH	C + H ₂	[300, 2000]	$2.7 \times 10^{-11} T_{32}^{0.38}$	51	H + O ⁺	O + H ⁺	[]	$5.66 \times 10^{-10} T_{32}^{0.36} \exp(\frac{8.6\text{K}}{T})$
2	H + CH ₂	CH + H ₂	[300, 2500]	6.64×10^{-11}	52	H ⁺ + O	O ⁺ + H	[, 10000]	$7.31 \times 10^{-10} T_{32}^{0.23} \exp(\frac{-225.9\text{K}}{T})$
3	H + CH ₃	CH ₂ + H ₂	[300, 2500]	$10^{-10} \exp(\frac{-7600\text{K}}{T})$	53	H ⁺ + H ₂ O	H ₂ O ⁺ + H	[, 300]	6.9×10^{-9}
4	H + CH ₄	CH ₃ + H ₂	[300, 2500]	$5.94 \times 10^{-13} T_{32}^{3.00} \exp(\frac{-4045\text{K}}{T})$	54	H ⁺ + O ₂	O ₂ ⁺ + H	[, 300]	2×10^{-9}
5	H + OH	O + H ₂	[300, 2500]	$6.98 \times 10^{-14} T_{32}^{2.80} \exp(\frac{-1950\text{K}}{T})$	55	H ₂ + He ⁺	He + H ₂ ⁺	[, 300]	7.19×10^{-15}
6	H + H ₂ O	OH + H ₂	[250, 3000]	$1.59 \times 10^{-11} T_{32}^{1.20} \exp(\frac{-9610\text{K}}{T})$	56	He ⁺ + C	C ⁺ + He	[, 300]	$6.29 \times 10^{-15} T_{32}^{0.75}$
7	H + CO	OH + C	[2590, 41000]	$1.09 \times 10^{-10} T_{32}^{0.50} \exp(\frac{-77700\text{K}}{T})$	57	O ⁺ + CO	CO ⁺ + O	[2000, 10000]	$4.89 \times 10^{-12} T_{32}^{0.50} \exp(\frac{-4580\text{K}}{T})$
8	H + O ₂	OH + O	[250, 4000]	$2.61 \times 10^{-10} \exp(\frac{-8156\text{K}}{T})$	58	H ₂ ⁺ + e ⁻	H + H	[, 300]	$1.6 \times 10^{-8} T_{32}^{-0.43}$
9	H ₂ + C	CH + H	[300, 2500]	$6.64 \times 10^{-10} \exp(\frac{-11700\text{K}}{T})$	59	H ₃ ⁺ + e ⁻	H + H + H	[, 1000]	$7.49 \times 10^{-8} T_{32}^{-0.30}$
10	H ₂ + CH	CH ₂ + H	[300, 2500]	$5.46 \times 10^{-10} \exp(\frac{-1943\text{K}}{T})$	60	H ₃ ⁺ + e ⁻	H ₂ + H	[, 1000]	$2.5 \times 10^{-8} T_{32}^{-0.30}$
11	H ₂ + CH ₂	CH ₃ + H	[300, 2500]	$5.18 \times 10^{-11} T_{32}^{0.17} \exp(\frac{-6400\text{K}}{T})$	61	CH ⁺ + e ⁻	C + H	[, 300]	$1.5 \times 10^{-7} T_{32}^{-0.42}$
12	H ₂ + CH ₃	CH ₄ + H	[300, 2500]	$6.86 \times 10^{-14} T_{32}^{2.74} \exp(\frac{-4740\text{K}}{T})$	62	CH ₂ ⁺ + e ⁻	CH + H	[, 10000]	$1.6 \times 10^{-7} T_{32}^{-0.60}$
13	H ₂ + O	OH + H	[297, 3532]	$3.14 \times 10^{-13} T_{32}^{2.70} \exp(\frac{-3150\text{K}}{T})$	63	CH ₂ ⁺ + e ⁻	C + H + H	[, 10000]	$4.03 \times 10^{-7} T_{32}^{-0.60}$
14	H ₂ + OH	H ₂ O + H	[250, 2581]	$2.04 \times 10^{-12} T_{32}^{1.52} \exp(\frac{-1736\text{K}}{T})$	64	CH ₂ ⁺ + e ⁻	C + H ₂	[, 10000]	$7.68 \times 10^{-8} T_{32}^{-0.60}$
15	H ₂ + O ₂	OH + OH	[300, 2500]	$3.15 \times 10^{-10} \exp(\frac{-21890\text{K}}{T})$	65	CH ₃ ⁺ + e ⁻	CH ₂ + H	[, 10000]	$1.4 \times 10^{-7} T_{32}^{-0.50}$
16	C + CH ₂	CH + CH	[1000, 4000]	$2.69 \times 10^{-12} \exp(\frac{-23550\text{K}}{T})$	66	CH ₃ ⁺ + e ⁻	CH + H ₂	[, 10000]	$4.9 \times 10^{-8} T_{32}^{-0.50}$
17	C + OH	O + CH	[493, 41000]	$2.25 \times 10^{-11} T_{32}^{0.50} \exp(\frac{-14800\text{K}}{T})$	67	CH ₃ ⁺ + e ⁻	CH + H + H	[, 10000]	$5.6 \times 10^{-8} T_{32}^{-0.50}$
18	C + OH	CO + H	[, 300]	$1.09 \times 10^{-10} T_{32}^{0.50}$	68	CH ₃ ⁺ + e ⁻	C + H ₂ + H	[, 10000]	$1.05 \times 10^{-7} T_{32}^{-0.5}$
19	C + O ₂	CO + O	[, 10000]	3.3×10^{-11}	69	CH ₄ ⁺ + e ⁻	CH ₃ + H	[, 300]	$1.75 \times 10^{-7} T_{32}^{-0.50}$
20	CH + O	OH + C	[, 6000]	$2.52 \times 10^{-11} \exp(\frac{-2381\text{K}}{T})$	70	CH ₄ ⁺ + e ⁻	CH ₂ + H + H	[, 300]	$1.75 \times 10^{-7} T_{32}^{-0.50}$
21	CH + O	CO + H	[, 2000]	6.6×10^{-11}	71	OH ⁺ + e ⁻	O + H	[, 300]	$3.74 \times 10^{-8} T_{32}^{-0.50}$
22	CH + CH ₄	CH ₃ + CH ₂	[100, 300]	$2.28 \times 10^{-11} T_{32}^{0.70} \exp(\frac{-3000\text{K}}{T})$	72	CH ₅ ⁺ + e ⁻	CH ₃ + H ₂	[, 300]	$5.5 \times 10^{-7} T_{32}^{-0.30}$
23	CH + O ₂	CO + OH	[298, 298]	2.6×10^{-11}	73	CH ₅ ⁺ + e ⁻	CH ₄ + H	[, 300]	$5.5 \times 10^{-7} T_{32}^{-0.30}$
24	CH ₂ + CH ₂	CH ₃ + CH	[300, 2500]	$4 \times 10^{-10} \exp(\frac{-5000\text{K}}{T})$	74	H ₂ O ⁺ + e ⁻	O + H + H	[, 10000]	$2.44 \times 10^{-7} T_{32}^{-0.50}$
25	CH ₂ + O	OH + CH	[1900, 2300]	$4.98 \times 10^{-10} \exp(\frac{-6000\text{K}}{T})$	75	H ₂ O ⁺ + e ⁻	O + H ₂	[, 10000]	$3.59 \times 10^{-8} T_{32}^{-0.50}$
26	CH ₂ + O	CO + H + H	[, 2500]	1.33×10^{-10}	76	H ₂ O ⁺ + e ⁻	OH + H	[, 10000]	$7.91 \times 10^{-8} T_{32}^{-0.50}$
27	CH ₂ + O	CO + H ₂	[1900, 2600]	8×10^{-11}	77	H ₃ O ⁺ + e ⁻	O + H ₂ + H	[, 10000]	$5.59 \times 10^{-9} T_{32}^{-0.50}$
28	CH ₂ + CH ₄	CH ₃ + CH ₃	[296, 2500]	$7.13 \times 10^{-12} \exp(\frac{-5050\text{K}}{T})$	78	H ₃ O ⁺ + e ⁻	OH + H + H	[, 10000]	$2.58 \times 10^{-7} T_{32}^{-0.50}$
29	CH ₂ + OH	O + CH ₃	[100, 300]	$1.44 \times 10^{-11} T_{32}^{0.50} \exp(\frac{-3000\text{K}}{T})$	79	H ₃ O ⁺ + e ⁻	OH + H ₂	[, 10000]	$6.45 \times 10^{-8} T_{32}^{-0.50}$
30	CH ₂ + OH	H ₂ O + CH	[100, 300]	$1.44 \times 10^{-11} T_{32}^{0.50} \exp(\frac{-3000\text{K}}{T})$	80	H ₃ O ⁺ + e ⁻	H ₂ O + H	[, 10000]	$1.08 \times 10^{-7} T_{32}^{-0.50}$
31	CH ₂ + O ₂	CO + H ₂ O	[1000, 1828]	$2.48 \times 10^{-10} T_{32}^{-3.30} \exp(\frac{-1443\text{K}}{T})$	81	CO ⁺ + e ⁻	O + C	[, 10000]	$2 \times 10^{-7} T_{32}^{-0.48}$
32	CH ₃ + CH ₃	CH ₄ + CH ₂	[1950, 2300]	$7.13 \times 10^{-12} \exp(\frac{-5052\text{K}}{T})$	82	HCO ⁺ + e ⁻	CO + H	[, 300]	$1.1 \times 10^{-7} T_{32}^{-1.00}$
33	CH ₃ + OH	CH ₄ + O	[298, 2500]	$3.27 \times 10^{-14} T_{32}^{2.20} \exp(\frac{-2240\text{K}}{T})$	83	O ₂ ⁺ + e ⁻	O + O	[, 300]	$1.95 \times 10^{-7} T_{32}^{-0.70}$
34	CH ₃ + OH	H ₂ O + CH ₂	[300, 1000]	$1.2 \times 10^{-10} \exp(\frac{-1400\text{K}}{T})$	84	H ⁺ + e ⁻	H	[, 20000]	$3.5 \times 10^{-12} T_{32}^{-0.75}$
35	CH ₃ + H ₂ O	OH + CH ₄	[300, 3000]	$2.29 \times 10^{-15} T_{32}^{3.47} \exp(\frac{-6681\text{K}}{T})$	85	He ⁺ + e ⁻	He	[, 300]	$2.36 \times 10^{-12} T_{32}^{-0.64}$
36	O + CH ₄	OH + CH ₃	[298, 2500]	$2.29 \times 10^{-12} T_{32}^{2.20} \exp(\frac{-3820\text{K}}{T})$	86	C ⁺ + e ⁻	C	[, 7950]	$4.67 \times 10^{-12} T_{32}^{-0.60}$
37	O + OH	O ₂ + H	[, 10000]	$4.34 \times 10^{-11} T_{32}^{-0.50} \exp(\frac{-30\text{K}}{T})$	87	CH ₃ ⁺ + e ⁻	CH ₃	[, 300]	$1.09 \times 10^{-10} T_{32}^{-0.50}$
38	O + H ₂ O	OH + OH	[300, 2500]	$1.85 \times 10^{-11} T_{32}^{0.95} \exp(\frac{-8571\text{K}}{T})$	88	O ⁺ + e ⁻	O	[]	$3.24 \times 10^{-12} T_{32}^{-0.66}$
39	CH ₄ + OH	H ₂ O + CH ₃	[178, 3000]	$3.77 \times 10^{-13} T_{32}^{2.42} \exp(\frac{-1162\text{K}}{T})$	89	H ⁺ + H	H ₂ ⁺	[200, 4000]	$5.13 \times 10^{-19} T_{32}^{1.85}$
40	OH + OH	H ₂ O + O	[, 10000]	$1.65 \times 10^{-12} T_{32}^{1.14} \exp(\frac{-50\text{K}}{T})$	90	H + C	CH	[, 300]	10^{-17}
41	H + CH ⁺	C ⁺ + H ₂	[, 300]	7.5×10^{-10}	91	H + C ⁺	CH ⁺	[, 300]	1.69×10^{-17}
42	H + CH ₂ ⁺	CH ⁺ + H ₂	[236, 300]	$10 \times 10^{-10} \exp(\frac{-7080\text{K}}{T})$	92	H + O	OH	[, 300]	$9.9 \times 10^{-19} T_{32}^{-0.38}$
43	H + CH ₃ ⁺	CH ₂ ⁺ + H ₂	[352, 41000]	$6.99 \times 10^{-10} \exp(\frac{-10560\text{K}}{T})$	93	H + OH	H ₂ O	[20, 300]	$5.26 \times 10^{-18} T_{32}^{-5.22} \exp(\frac{-90\text{K}}{T})$
44	H ₂ + He ⁺	He + H ⁺ + H	[, 300]	$3.7 \times 10^{-14} \exp(\frac{-35\text{K}}{T})$	94	H ₂ + C	CH ₂	[, 300]	10^{-17}
45	H ₂ + C ⁺	CH ⁺ + H	[154, 300]	$10^{-10} \exp(\frac{-4640\text{K}}{T})$	95	H ₂ + C ⁺	CH ₂ ⁺	[, 300]	$4 \times 10^{-16} T_{32}^{-0.20}$
46	H ₂ + CH ⁺	CH ₂ ⁺ + H	[, 300]	1.2×10^{-9}	96	H ₂ + CH	CH ₃	[, 300]	$5.09 \times 10^{-18} T_{32}^{-0.71} \exp(\frac{-11.6\text{K}}{T})$
47	He ⁺ + CO	O ⁺ + C + He	[2000, 10000]	$1.4 \times 10^{-16} T_{32}^{-0.50}$	97	H ₂ + CH ₃ ⁺	CH ₅ ⁺	[, 300]	$1.3 \times 10^{-14} T_{32}^{-1.00}$
48	C ⁺ + OH	CO + H ⁺	[, 10000]	7.7×10^{-10}	98	C + O	CO	[, 300]	2.1×10^{-19}
49	H ⁺ + H ₂	H ₂ ⁺ + H	[706, 41000]	$10^{-10} \exp(\frac{-21200\text{K}}{T})$	99	C ⁺ + O	CO ⁺	[, 300]	2.5×10^{-18}
50	H + He ⁺	He + H ⁺	[, 1000]	$4.84 \times 10^{-15} T_{32}^{0.18}$	100	O + O	O ₂	[, 300]	$4.9 \times 10^{-20} T_{32}^{1.58}$

Table G1. Chemical network employed in V1 and V4 benchmark tests. Temperature limits are in K, [] indicates no temperature limits, while e.g. [, 300] and [50,] indicate that there are no lower and upper limits, respectively. Note that in the benchmark we arbitrarily extended the temperature limits reported here for completeness. Two-body reaction rate coefficients are in units of cm³ s⁻¹, photochemical and cosmic-rays reactions in s⁻¹. $T_{32} = T/300$ K. A detailed analysis of the network will be presented in Paper II. Table [continues](#) in Tab. [G2](#).

101 H + H ₂	H + H + H	[1833, 41000]	$4.67 \times 10^{-7} T_{32}^{-1.00} \exp\left(\frac{-55000 \text{ K}}{T}\right)$	151 He ⁺ + OH	O ⁺ + He + H	[]	1.09×10^{-9}
102 H + CH	C + H + H	[1340, 41000]	$6 \times 10^{-9} \exp\left(\frac{-40200 \text{ K}}{T}\right)$	152 He ⁺ + H ₂ O	OH + He + H ⁺	[]	2.04×10^{-10}
103 H + OH	O + H + H	[1696, 41000]	$6 \times 10^{-9} \exp\left(\frac{-50900 \text{ K}}{T}\right)$	153 He ⁺ + H ₂ O	OH ⁺ + He + H	[]	2.86×10^{-10}
104 H + H ₂ O	OH + H + H	[1763, 41000]	$5.8 \times 10^{-9} \exp\left(\frac{-52900 \text{ K}}{T}\right)$	154 He ⁺ + CO	O + C ⁺ + He	[]	1.6×10^{-9}
105 H + O ₂	O + O + H	[1743, 41000]	$6 \times 10^{-9} \exp\left(\frac{-52300 \text{ K}}{T}\right)$	155 He ⁺ + O ₂	O ⁺ + O + He	[]	10^{-9}
106 H ₂ + e ⁻	H + H + e ⁻	[3400, 41000]	$3.22 \times 10^{-9} T_{32}^{0.35} \exp\left(\frac{-102000 \text{ K}}{T}\right)$	156 C + OH ⁺	O + CH ⁺	[]	1.2×10^{-9}
107 H ₂ + H ₂	H ₂ + H + H	[2803, 41000]	$10^{-8} \exp\left(\frac{-84100 \text{ K}}{T}\right)$	157 C ⁺ + OH	CO ⁺ + H	[]	7.7×10^{-10}
108 H ₂ + CH	C + H ₂ + H	[1340, 41000]	$6 \times 10^{-9} \exp\left(\frac{-40200 \text{ K}}{T}\right)$	158 C + CH ₅ ⁺	CH ₄ + CH ⁺	[]	1.2×10^{-9}
109 H ₂ + OH	O + H ₂ + H	[1696, 41000]	$6 \times 10^{-9} \exp\left(\frac{-50900 \text{ K}}{T}\right)$	159 C + H ₂ O ⁺	OH + CH ⁺	[]	1.09×10^{-9}
110 H ₂ + H ₂ O	OH + H ₂ + H	[1763, 41000]	$5.8 \times 10^{-9} \exp\left(\frac{-52900 \text{ K}}{T}\right)$	160 C ⁺ + H ₂ O	HCO ⁺ + H	[]	9×10^{-10}
111 H ₂ + O ₂	O + O + H ₂	[1743, 41000]	$6 \times 10^{-9} \exp\left(\frac{-52300 \text{ K}}{T}\right)$	161 C + H ₃ O ⁺	HCO ⁺ + H ₂	[]	10^{-11}
112 CH + O	HCO ⁺ + e ⁻	[, 1750]	$2 \times 10^{-11} T_{32}^{0.44}$	162 C + HCO ⁺	CO + CH ⁺	[]	1.09×10^{-9}
113 H + H	H ₂	[]	see text	163 C ⁺ + O ₂	CO ⁺ + O	[]	3.8×10^{-10}
114 H ⁺ + CH ₂	CH ⁺ + H ₂	[]	1.4×10^{-9}	164 C ⁺ + O ₂	CO + O ⁺	[]	6.2×10^{-10}
115 H ⁺ + CH ₄	CH ₃ ⁺ + H ₂	[]	2.29×10^{-9}	165 C + O ₂ ⁺	CO ⁺ + O	[]	5.2×10^{-11}
116 H + CH ₄ ⁺	CH ₃ ⁺ + H ₂	[]	10^{-11}	166 CH ⁺ + O	CO ⁺ + H	[]	3.49×10^{-10}
117 H + CH ₅ ⁺	CH ₄ ⁺ + H ₂	[]	2×10^{-11}	167 CH + O ⁺	CO ⁺ + H	[]	3.49×10^{-10}
118 H ₂ ⁺ + H ₂	H ₃ ⁺ + H	[]	2.07×10^{-9}	168 CH + OH ⁺	O + CH ₂ ⁺	[]	3.49×10^{-10}
119 H ₂ ⁺ + C	CH ⁺ + H	[]	2.4×10^{-9}	169 CH ⁺ + OH	CO ⁺ + H ₂	[]	7.5×10^{-10}
120 H ₂ ⁺ + CH	CH ₂ ⁺ + H	[]	7.1×10^{-10}	170 CH + CH ₅ ⁺	CH ₄ + CH ₂ ⁺	[]	6.9×10^{-10}
121 H ₂ ⁺ + CH ₂	CH ₃ ⁺ + H	[]	10^{-9}	171 CH ⁺ + H ₂ O	H ₃ O ⁺ + C	[]	5.8×10^{-10}
122 H ₂ + CH ₂ ⁺	CH ₃ ⁺ + H	[]	1.6×10^{-9}	172 CH + H ₂ O ⁺	OH + CH ₂ ⁺	[]	3.4×10^{-10}
123 H ₂ ⁺ + O	OH ⁺ + H	[]	1.5×10^{-9}	173 CH ⁺ + H ₂ O	HCO ⁺ + H ₂	[]	2.9×10^{-9}
124 H ₂ + O ⁺	OH ⁺ + H	[]	1.69×10^{-9}	174 CH + H ₃ O ⁺	H ₂ O + CH ₂ ⁺	[]	6.8×10^{-10}
125 H ₂ ⁺ + CH ₄	CH ₅ ⁺ + H	[]	1.13×10^{-10}	175 CH + CO ⁺	HCO ⁺ + C	[]	3.2×10^{-10}
126 H ₂ + CH ₄ ⁺	CH ₅ ⁺ + H	[]	3.3×10^{-11}	176 CH + HCO ⁺	CO + CH ₂ ⁺	[]	6.3×10^{-10}
127 H ₂ ⁺ + CH ₄	CH ₃ ⁺ + H ₂ + H	[]	2.29×10^{-9}	177 CH ⁺ + O ₂	CO ⁺ + OH	[]	10^{-11}
128 H ₂ ⁺ + OH	H ₂ O ⁺ + H	[]	7.6×10^{-10}	178 CH ⁺ + O ₂	HCO ⁺ + O	[]	9.69×10^{-10}
129 H ₂ + OH ⁺	H ₂ O ⁺ + H	[]	1.01×10^{-9}	179 CH + O ₂ ⁺	HCO ⁺ + O	[]	3.1×10^{-10}
130 H ₂ ⁺ + H ₂ O	H ₃ O ⁺ + H	[]	3.39×10^{-9}	180 CH ₂ ⁺ + O	HCO ⁺ + H	[]	7.5×10^{-10}
131 H ₂ + H ₂ O ⁺	H ₃ O ⁺ + H	[]	6.4×10^{-10}	181 CH ₂ + OH ⁺	O + CH ₃ ⁺	[]	4.8×10^{-10}
132 H ₂ ⁺ + CO	HCO ⁺ + H	[]	2.15×10^{-9}	182 CH ₂ + CH ₅ ⁺	CH ₄ + CH ₃ ⁺	[]	9.6×10^{-10}
133 H ₂ + CO ⁺	HCO ⁺ + H	[]	1.79×10^{-9}	183 CH ₂ + H ₂ O ⁺	OH + CH ₃ ⁺	[]	4.7×10^{-10}
134 H ₃ ⁺ + C	CH ⁺ + H ₂	[]	2×10^{-9}	184 CH ₂ + H ₃ O ⁺	H ₂ O + CH ₃ ⁺	[]	9.4×10^{-10}
135 H ₃ ⁺ + CH	CH ₂ ⁺ + H ₂	[]	1.2×10^{-9}	185 CH ₂ + CO ⁺	HCO ⁺ + CH	[]	4.3×10^{-10}
136 H ₃ ⁺ + CH ₂	CH ₃ ⁺ + H ₂	[]	1.69×10^{-9}	186 CH ₂ + HCO ⁺	CO + CH ₃ ⁺	[]	8.6×10^{-10}
137 H ₃ ⁺ + CH ₃	CH ₄ ⁺ + H ₂	[]	2.1×10^{-9}	187 CH ₂ ⁺ + O ₂	HCO ⁺ + OH	[]	9.1×10^{-10}
138 H ₃ ⁺ + O	OH ⁺ + H ₂	[]	8×10^{-10}	188 CH ₃ ⁺ + O	HCO ⁺ + H ₂	[]	4×10^{-10}
139 H ₃ ⁺ + CH ₄	CH ₅ ⁺ + H ₂	[]	2.4×10^{-9}	189 O ⁺ + CH ₄	OH + CH ₃ ⁺	[]	1.09×10^{-10}
140 H ₃ ⁺ + OH	H ₂ O ⁺ + H ₂	[]	1.3×10^{-9}	190 O + CH ₄ ⁺	OH + CH ₃ ⁺	[]	10^{-9}
141 H ₃ ⁺ + H ₂ O	H ₃ O ⁺ + H ₂	[]	5.9×10^{-9}	191 O ⁺ + OH	O ₂ ⁺ + H	[]	3.59×10^{-10}
142 H ₃ ⁺ + CO	HCO ⁺ + H ₂	[]	1.69×10^{-9}	192 O + OH ⁺	O ₂ ⁺ + H	[]	7.1×10^{-10}
143 He ⁺ + CH	C ⁺ + He + H	[]	1.09×10^{-9}	193 O + CH ₅ ⁺	H ₃ O ⁺ + CH ₂	[]	2.19×10^{-10}
144 He ⁺ + CH ₂	C ⁺ + He + H ₂	[]	7.5×10^{-10}	194 O + H ₂ O ⁺	O ₂ ⁺ + H ₂	[]	4×10^{-11}
145 He ⁺ + CH ₂	CH ⁺ + He + H	[]	7.5×10^{-10}	195 CH ₄ ⁺ + CH ₄	CH ₅ ⁺ + CH ₃	[]	1.5×10^{-9}
146 He ⁺ + CH ₃	CH ⁺ + He + H ₂	[]	1.79×10^{-9}	196 CH ₄ + OH ⁺	CH ₅ ⁺ + O	[]	1.95×10^{-10}
147 He ⁺ + CH ₄	CH ⁺ + He + H ₂ + H	[]	2.4×10^{-10}	197 CH ₄ + OH ⁺	H ₃ O ⁺ + CH ₂	[]	1.31×10^{-9}
148 He ⁺ + CH ₄	CH ₂ ⁺ + He + H ₂	[]	9.5×10^{-10}	198 CH ₄ ⁺ + H ₂ O	H ₃ O ⁺ + CH ₃	[]	2.6×10^{-9}
149 He ⁺ + CH ₄	CH ₃ + He + H ⁺	[]	4.8×10^{-10}	199 CH ₄ + H ₂ O ⁺	H ₃ O ⁺ + CH ₃	[]	1.4×10^{-9}
150 He ⁺ + CH ₄	CH ₃ ⁺ + He + H	[]	8.5×10^{-11}	200 CH ₄ ⁺ + CO	HCO ⁺ + CH ₃	[]	1.4×10^{-9}

Table G2. Chemical network employed in V1 and V4 benchmark tests. Continued from Tab. G1, [continues](#) in Tab. G3. More details in Tab. G1.

APPENDIX H: V1 MODEL WITH ENHANCED DENSITY

To determine the behaviour of the code in an environment similar to what can be found for example in the deeper region of a molecular cloud, we increased the density of the model V1 to $n_{\text{gas}} = 10^8 \text{ cm}^{-3}$, and extended the maximum visual extinction to $A_v = 100$, with 1000 spatial grid points. As shown in Fig. H1, at higher A_v the radiation becomes almost ineffective, and the only sources of heating are cosmic rays (since ζ is assumed constant), and the chemical heating due to the formation of molecular hydrogen on dust grains. Analogously, dust cooling dominates the thermal budget, and from Eq. (44) and Eq. (45) the solution of the heating-cooling balance is then $T \simeq T_d$, as shown in Fig. H2.

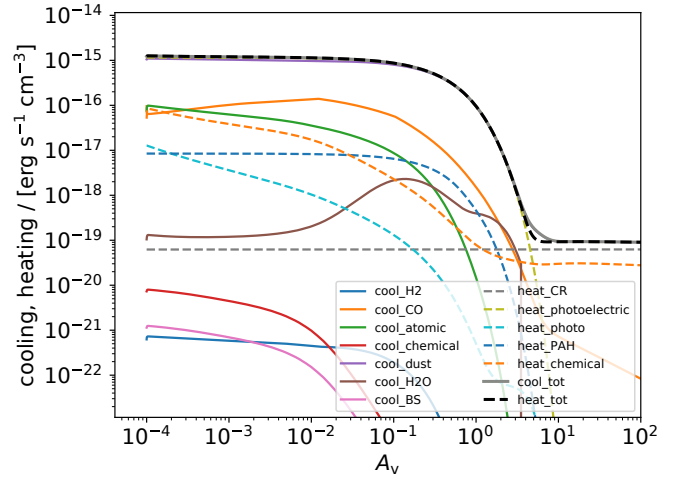


Figure H1. Model V1 with enhanced density. Cooling (solid) and heating (dashed) functions at different visual extinction values. Grey solid and black dashed lines indicate the sum of the cooling (`cool_tot`) and heating terms (`heat_tot`), respectively. In this model $n_{\text{gas}} = 10^8 \text{ cm}^{-3}$ and $A_v = 100$.

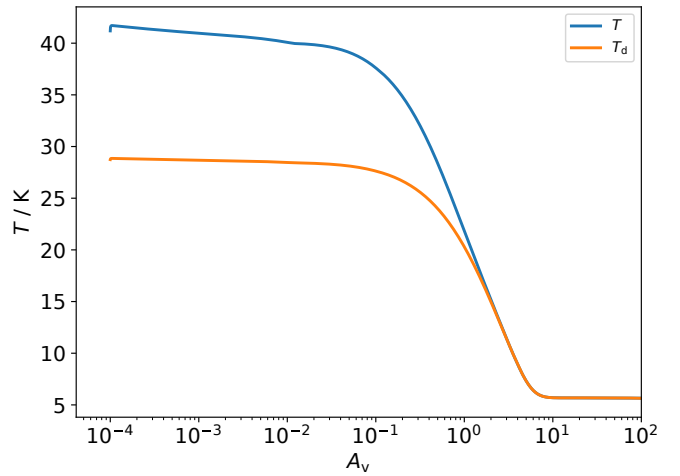


Figure H2. Model V1 with enhanced density. Gas (blue) and dust (orange) temperature profiles as a function of the visual extinction A_v . In this model $n_{\text{gas}} = 10^8 \text{ cm}^{-3}$ and $A_v = 100$.

201	CH ₄ + CO ⁺	HCO ⁺ + CH ₃	[]	4.55 × 10 ⁻¹⁰	251	O ⁺ + O ₂	O ₂ ⁺ + O	[]	1.9 × 10 ⁻¹¹
202	OH ⁺ + OH	H ₂ O ⁺ + O	[]	6.99 × 10 ⁻¹⁰	252	CH ₄ + CO ⁺	CO + CH ₄ ⁺	[]	7.92 × 10 ⁻¹⁰
203	OH + CH ₅ ⁺	H ₂ O ⁺ + CH ₄	[]	6.99 × 10 ⁻¹⁰	253	CH ₄ ⁺ + O ₂	O ₂ ⁺ + CH ₄	[]	4 × 10 ⁻¹⁰
204	OH ⁺ + H ₂ O	H ₃ O ⁺ + O	[]	1.3 × 10 ⁻⁹	254	OH ⁺ + H ₂ O	H ₂ O ⁺ + OH	[]	1.59 × 10 ⁻⁹
205	OH + H ₂ O ⁺	H ₃ O ⁺ + O	[]	6.9 × 10 ⁻¹⁰	255	OH + CO ⁺	CO + OH ⁺	[]	3.1 × 10 ⁻¹⁰
206	OH ⁺ + CO	HCO ⁺ + O	[]	1.05 × 10 ⁻⁹	256	OH ⁺ + O ₂	O ₂ ⁺ + OH	[]	5.9 × 10 ⁻¹⁰
207	OH + CO ⁺	HCO ⁺ + O	[]	3.1 × 10 ⁻¹⁰	257	H ₂ O + CO ⁺	CO + H ₂ O ⁺	[]	1.72 × 10 ⁻⁹
208	OH + HCO ⁺	CO + H ₂ O ⁺	[]	6.2 × 10 ⁻¹⁰	258	H ₂ O ⁺ + O ₂	O ₂ ⁺ + H ₂ O	[]	4.59 × 10 ⁻¹⁰
209	CH ₅ ⁺ + H ₂ O	H ₃ O ⁺ + CH ₄	[]	3.7 × 10 ⁻⁹	259	CO ⁺ + O ₂	O ₂ ⁺ + CO	[]	1.2 × 10 ⁻¹⁰
210	CH ₅ ⁺ + CO	HCO ⁺ + CH ₄	[]	10 ⁻⁹	260	H ₂ + γ	H + H	[]	see text
211	H ₂ O ⁺ + H ₂ O	H ₃ O ⁺ + OH	[]	2.1 × 10 ⁻⁹	261	CO + γ	C + O	[]	see text
212	H ₂ O ⁺ + CO	HCO ⁺ + OH	[]	5 × 10 ⁻¹⁰	262	H ₂ ⁺ + γ	H ⁺ + H	[]	see text
213	H ₂ O + CO ⁺	HCO ⁺ + OH	[]	8.84 × 10 ⁻¹⁰	263	H ₃ ⁺ + γ	H ₂ ⁺ + H	[]	see text (branch ratio 0.5, KIDA)
214	H ₂ O + HCO ⁺	CO + H ₃ O ⁺	[]	2.5 × 10 ⁻⁹	264	H ₃ ⁺ + γ	H ₂ + H ⁺	[]	see text (branch ratio 0.5, KIDA)
215	H + H ₂ ⁺	H ₂ + H ⁺	[]	6.4 × 10 ⁻¹⁰	265	C + γ	C ⁺ + e ⁻	[]	see text
216	H ⁺ + CH	CH ⁺ + H	[]	1.9 × 10 ⁻⁹	266	CH + γ	CH ⁺ + e ⁻	[]	see text
217	H ⁺ + CH ₂	CH ₂ ⁺ + H	[]	1.4 × 10 ⁻⁹	267	CH + γ	C + H	[]	see text
218	H ⁺ + CH ₃	CH ₃ ⁺ + H	[]	3.39 × 10 ⁻⁹	268	CH ⁺ + γ	C ⁺ + H	[]	see text
219	H ⁺ + CH ₄	CH ₄ ⁺ + H	[]	1.5 × 10 ⁻⁹	269	CH ₂ + γ	CH ₂ ⁺ + e ⁻	[]	see text
220	H ⁺ + OH	OH ⁺ + H	[]	2.1 × 10 ⁻⁹	270	CH ₂ + γ	CH + H	[]	see text
221	H + CO ⁺	CO + H ⁺	[]	7.5 × 10 ⁻¹⁰	271	CH ₂ ⁺ + γ	CH ⁺ + H	[]	see text
222	H ₂ ⁺ + CH	CH ⁺ + H ₂	[]	7.1 × 10 ⁻¹⁰	272	CH ₃ + γ	CH ₃ ⁺ + e ⁻	[]	see text
223	H ₂ ⁺ + CH ₂	CH ₂ ⁺ + H ₂	[]	10 ⁻⁹	273	CH ₃ + γ	CH ₂ + H	[]	see text
224	H ₂ ⁺ + CH ₄	CH ₄ ⁺ + H ₂	[]	1.4 × 10 ⁻⁹	274	CH ₃ + γ	CH + H ₂	[]	see text
225	H ₂ ⁺ + OH	OH ⁺ + H ₂	[]	7.6 × 10 ⁻¹⁰	275	CH ₄ + γ	CH ₃ + H	[]	see text
226	H ₂ ⁺ + H ₂ O	H ₂ O ⁺ + H ₂	[]	3.9 × 10 ⁻⁹	276	CH ₄ + γ	CH ₂ + H ₂	[]	see text
227	H ₂ ⁺ + CO	CO ⁺ + H ₂	[]	6.4 × 10 ⁻¹⁰	277	CH ₄ + γ	CH + H ₂ + H	[]	see text
228	H ₂ ⁺ + O ₂	O ₂ ⁺ + H ₂	[]	8 × 10 ⁻¹⁰	278	OH + γ	OH ⁺ + e ⁻	[]	see text
229	He ⁺ + CH	CH ⁺ + He	[]	5 × 10 ⁻¹⁰	279	OH + γ	O + H	[]	see text
230	He ⁺ + CH ₄	CH ₄ ⁺ + He	[]	5.1 × 10 ⁻¹¹	280	OH ⁺ + γ	O + H ⁺	[]	see text
231	He ⁺ + H ₂ O	H ₂ O ⁺ + He	[]	6.05 × 10 ⁻¹¹	281	H ₂ O + γ	OH + H	[]	see text
232	He ⁺ + O ₂	O ₂ ⁺ + He	[]	3.3 × 10 ⁻¹¹	282	H ₂ O + γ	H ₂ O ⁺ + e ⁻	[]	see text
233	C ⁺ + CH	CH ⁺ + C	[]	3.8 × 10 ⁻¹⁰	283	O ₂ + γ	O + O	[]	see text
234	C ⁺ + CH ₂	CH ₂ ⁺ + C	[]	5.19 × 10 ⁻¹⁰	284	O ₂ + γ	O ₂ ⁺ + e ⁻	[]	see text
235	C + CO ⁺	CO + C ⁺	[]	1.09 × 10 ⁻¹⁰	285	H ₂ + CR	H ⁺ + H + e ⁻	[]	2 × 10 ⁻² ζ
236	C + O ₂ ⁺	O ₂ + C ⁺	[]	5.2 × 10 ⁻¹¹	286	H ₂ + CR	H + H	[]	10 ⁻¹ ζ
237	CH + O ⁺	O + CH ⁺	[]	3.49 × 10 ⁻¹⁰	287	H ₂ + CR	H ₂ ⁺ + e ⁻	[]	8.79 × 10 ⁻¹ ζ
238	CH + OH ⁺	OH + CH ⁺	[]	3.49 × 10 ⁻¹⁰	288	H + CR	H ⁺ + e ⁻	[]	4.59 × 10 ⁻¹ ζ
239	CH + H ₂ O ⁺	H ₂ O + CH ⁺	[]	3.4 × 10 ⁻¹⁰	289	He + CR	He ⁺ + e ⁻	[]	5 × 10 ⁻¹ ζ
240	CH + CO ⁺	CO + CH ⁺	[]	3.2 × 10 ⁻¹⁰					
241	CH + O ₂ ⁺	O ₂ + CH ⁺	[]	3.1 × 10 ⁻¹⁰					
242	CH ₂ + O ⁺	O + CH ₂ ⁺	[]	9.69 × 10 ⁻¹⁰					
243	CH ₂ + OH ⁺	OH + CH ₂ ⁺	[]	4.8 × 10 ⁻¹⁰					
244	CH ₂ + H ₂ O ⁺	H ₂ O + CH ₂ ⁺	[]	4.7 × 10 ⁻¹⁰					
245	CH ₂ + CO ⁺	CO + CH ₂ ⁺	[]	4.3 × 10 ⁻¹⁰					
246	CH ₂ + O ₂ ⁺	O ₂ + CH ₂ ⁺	[]	4.3 × 10 ⁻¹⁰					
247	O ⁺ + CH ₄	CH ₄ ⁺ + O	[]	8.9 × 10 ⁻¹⁰					
248	O ⁺ + OH	OH ⁺ + O	[]	3.59 × 10 ⁻¹⁰					
249	O ⁺ + H ₂ O	H ₂ O ⁺ + O	[]	3.2 × 10 ⁻⁹					
250	O + CO ⁺	CO + O ⁺	[]	1.4 × 10 ⁻¹⁰					

Table G3. Chemical network employed in V1 and V4 benchmark tests. Continued from Tab. G2, more details in Tab. G1.

APPENDIX I: X-RAY MOLECULAR REACTIONS

The photochemical reactions of molecular species when X-ray photons are present, are computed summing the cross-sections of individual atomic species, following the criteria of [Ádámkóvics et al. \(2011\)](#). The cross sections are reported in Tab. II, where the atomic cross sections $\sigma_{i,j}$ are for the i th species and the j th electronic shell.

This paper has been typeset from a $\text{\TeX}/\text{\LaTeX}$ file prepared by the author.

Molecular cross-section	Mixing criterion
$\text{CO} \rightarrow \text{C}^+ + \text{O}^+ + 2\text{e}^-$	$0.5(\sigma_{\text{C,K}} + \sigma_{\text{C,L}} + \sigma_{\text{O,K}} + \sigma_{\text{O,L}})$
$\text{H}_2\text{O} \rightarrow \text{O}^{++} + 2\text{H} + 2\text{e}^-$	$\sigma_{\text{H,K}} + \sigma_{\text{H,L}} + \sigma_{\text{O,K}}$
$\text{H}_2\text{O} \rightarrow \text{O}^+ + 2\text{H} + \text{e}^-$	$\sigma_{\text{O,L}}$
$\text{OH} \rightarrow \text{O}^{++} + \text{H} + 2\text{e}^-$	$\sigma_{\text{O,K}} + \sigma_{\text{H,K}}$
$\text{OH} \rightarrow \text{O}^+ + \text{H} + \text{e}^-$	$\sigma_{\text{O,L}}$
$\text{N}_2 \rightarrow \text{N}^+ + \text{N} + \text{e}^-$	$\sigma_{\text{N,L}} + \sigma_{\text{N,L}}$
$\text{N}_2 \rightarrow \text{N}^{++} + \text{N} + 2\text{e}^-$	$\sigma_{\text{N,K}} + \sigma_{\text{N,K}}$
$\text{O}_2 \rightarrow \text{O}^+ + \text{O} + \text{e}^-$	$\sigma_{\text{O,L}} + \sigma_{\text{O,L}}$
$\text{O}_2 \rightarrow \text{O}^{++} + \text{O} + 2\text{e}^-$	$\sigma_{\text{O,K}} + \sigma_{\text{O,K}}$
$\text{CH}_2 \rightarrow \text{C}^{++} + 2\text{H} + 2\text{e}^-$	$\sigma_{\text{C,K}}$
$\text{NH}_2 \rightarrow \text{N}^{++} + 2\text{H} + 2\text{e}^-$	$\sigma_{\text{N,K}}$
$\text{CH}_3 \rightarrow \text{C}^{++} + 3\text{H} + 2\text{e}^-$	$\sigma_{\text{C,K}}$
$\text{NH}_3 \rightarrow \text{N}^{++} + 3\text{H} + 2\text{e}^-$	$\sigma_{\text{N,K}}$
$\text{CH}_4 \rightarrow \text{C}^{++} + 4\text{H} + 2\text{e}^-$	$\sigma_{\text{C,K}}$
$\text{NH}_4 \rightarrow \text{N}^{++} + 4\text{H} + 2\text{e}^-$	$\sigma_{\text{N,K}}$
$\text{CN} \rightarrow \text{C}^{++} + \text{N} + 2\text{e}^-$	$\sigma_{\text{C,K}}$
$\text{CN} \rightarrow \text{C} + \text{N}^{++} + 2\text{e}^-$	$\sigma_{\text{N,K}}$
$\text{CN} \rightarrow \text{C}^+ + \text{N}^+ + 2\text{e}^-$	$\sigma_{\text{C,L}} + \sigma_{\text{N,L}}$
$\text{NO} \rightarrow \text{N}^{++} + \text{O} + 2\text{e}^-$	$\sigma_{\text{N,K}}$
$\text{NO} \rightarrow \text{N} + \text{O}^{++} + 2\text{e}^-$	$\sigma_{\text{O,K}}$
$\text{NO} \rightarrow \text{N}^+ + \text{O}^+ + 2\text{e}^-$	$\sigma_{\text{N,L}} + \sigma_{\text{O,L}}$
$\text{SiH} \rightarrow \text{Si}^+ + \text{H} + \text{e}^-$	$\sigma_{\text{Si,K}}$
$\text{SiO} \rightarrow \text{Si}^+ + \text{O}^+ + 2\text{e}^-$	$\text{Si}_\text{L} + \sigma_{\text{O,L}}$
$\text{SiO} \rightarrow \text{Si} + \text{O}^{++} + 2\text{e}^-$	$\sigma_{\text{O,K}}$
$\text{HCN} \rightarrow \text{C}^{++} + \text{NH} + 2\text{e}^-$	$\sigma_{\text{C,K}}$
$\text{HCN} \rightarrow \text{N}^{++} + \text{CH} + 2\text{e}^-$	$\sigma_{\text{N,K}}$
$\text{CO}_2 \rightarrow \text{C}^{++} + \text{O}_2 + 2\text{e}^-$	$\sigma_{\text{C,K}}$
$\text{CO}_2 \rightarrow \text{O}^{++} + \text{CO} + 2\text{e}^-$	$\sigma_{\text{O,K}} + \sigma_{\text{O,K}}$

Table II. Mixing criteria for the cross-sections employed for molecular photochemistry in the presence of X-rays, where $\sigma_{i,j}$ is the cross-section of the j th electronic shell of the i th atomic species.